

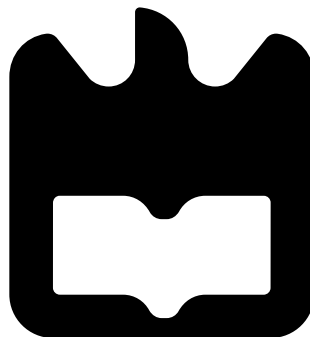


João Diogo

Victor Fernandes

**Transformada de Haar baseada num Interferómetro
Multimodo 2 x 2**

**Haar Transform based on a 2 x 2 Multimode
Interferometer**





João Diogo

Victor Fernandes

**Haar Transform based on a 2 x 2 Multimode
Interferometer**

Dissertação apresentada à Universidade de Aveiro para cumprimento dos requisitos necessários à obtenção do grau de Mestre em Engenharia Electrónica e Telecomunicações, realizada sob a orientação científica de Dr. António Teixeira e Dr. Mário Lima, Professores do Departamento de Electrónica Telecomunicações e Informática da Universidade de Aveiro

'Intelligence is the ability to adapt to change' - Stephen Hawking

o júri / the jury

presidente / president

Professor Doutor Paulo Miguel Nepomuceno Pereira Monteiro

Professor Associado da Universidade de Aveiro

vogais / examiners committee

Professora Doutora Maria do Carmo Raposo de Medeiros

Professora Associada da Universidade de Coimbra

Professor Doutor Mário José Neves de Lima

Professor Auxiliar da Universidade de Aveiro

agradecimentos

Aos professores António Teixeira e Mário Lima, um obrigado pela orientação ao longo deste ano que passou, por todo o conhecimento científico e pela autonomia que me inculcaram e permitiram ter que me ajudou a crescer na área.

À minha família por todo o apoio dado nos altos e baixos deste meu percurso. Sem vocês não estava onde estou e não era a pessoa que sou agora. Mais concretamente aos meus pais e irmã, tendo consciência que sozinho nada disto era possível, do fundo do meu coração, um beijo sincero de obrigado. Obrigado por fazerem de mim este bom idota que sou.

À família que a cidade de Aveiro me deu, Sequeira, Lhé, Taveira, Tomé, Carla, Inês, Alpha, Gonçalo, Ricardo e Jorge, são muitas as palavras que podia dizer para vos agradecer. Solta-se aquela lágrima ao recordar tudo o que passamos nestes 6 anos. Que venham mais 60 anos ao vosso lado.

Ao Francisco, um enorme obrigado. Sem ti andava devagar devagarinho. Ajudaste-me a quebrar barreiras, a solucionar problemas e o conhecimento que me proporcionaste foi sem dúvida o que mais me ajudou a concluir esta etapa.

À Tuna Universitária de Aveiro. O meu lazer, o meu vício, a minha calma e a minha paz. Aqui encontrei a maneira mais pura de me abstrair dos meus problemas. Dedico ao Jendrix e ao Sebastião um obrigado ainda maior, por me aturarem das 9h as 9h durante tantos dias na sala. Sem vocês era mais difícil.

Por último a ti Catarina, o meu mais especial obrigado. Foste o meu porto seguro e o meu apoio quando mais precisei. Nunca me falhaste e deste-me sempre força para ultrapassar as minhas dificuldades e obstáculos. Não há palavras para explicar a tua importância e a presença que tiveste nesta minha fase.

palavras-chave

Fotónica, Interferómetro Multimodo, Guia de Ondas, Óptica integrada, Self-imaging, Magic-T, Transformada de Ondas de Haar

resumo

Com o crescimento de novos dispositivos fotónicos resultantes da junção da electrónica e óptica, surgiram novas áreas de estudo. A fotónica integrada é uma dessas áreas e refere-se ao fabrico e implementação de vários componentes fotónicos num substrato plano comum. De forma a obter um processamento de imagem superior, os métodos de compressão são uma ferramenta fundamental, da qual a transformada de Haar é a mais importante devido a sua facilidade de implementação e rápida computação. Este método pode ser alcançado com o uso de estruturas ópticas. Com isto, a implementação da transformada com um dispositivo óptico é desenvolvida nesta dissertação. Os Interferómetros Multimodo são guias de onda com N entradas e M saídas, e são apresentados como uma possível solução para conseguir a transformada de Haar. Isto vai permitir criar a soma e a subtração de sinais fundamental à transformada de Haar. Magic-T é o nome dado ao dispositivo que possui esta capacidade de soma e subtração. O estudo teórico feito por Soldano et al. e algumas implementações de Magic-T com diferentes dispositivos ópticos são analisados. Com a informação reunida e baseada em diferentes arquitecturas apresentadas por Besse et al. e El-Sabban et al. uma solução final foi obtida com o uso de um Interferómetro Multimodo 2×2 . Através do uso de simulações de Método de Propagação de Feixe no OptoDesigner Phoenix SoftwareTM a solução foi analisada e optimizada. Algumas comparações são feitas com os dispositivos Magic-T já analisados. No fim é implementada uma rede de Haar com o Magic-T projectado e são feitas novas simulações sobre esta rede, concluindo que é uma solução viável e um possível substituto a alguns componentes já implementados com outros Magic-T. Este componente vai ser integrado no âmbito do projecto COMPRESS de forma a substituir um acoplador que realiza também a transformada de Haar.

keywords

Photonics, Multimode Interferometer, Waveguides, Integrated optics, Self-imaging, Magic-T, Haar Wavelet Transform

abstract

The arising of new photonic devices resulting from the connection of electronics and optics, new areas of study were created. Integrated photonics is one of those areas and it refers to the fabrication and integration of several photonics components on a common planar substrate. In order to obtain a superior image processing, the compression methods are a fundamental tool, in which the Haar Wavelet Transform is the most used due to the uncomplicated design and also fast computation. This method of compression can be achieved with optical structures. With this background, an Haar transform implementation with an optical tool is developed in this thesis. Multimode Interferometers are a waveguide structure with N inputs and M outputs, and are presented as a solution to achieve the Haar Transform. This device will allow to make signal additions and differences required by the Haar Transform and when having this proprieties it is named as Magic-T. The theoretical approach made by Soldano et al. and other Magic-T implementations with various optical devices are analysed. With the information gathered and inspired in different architectures made by Besse et al. and El-Sabban et al. a final solution was achieved with the use of an 2×2 Multimode Interferometer. Through Beam Propagation Method simulations on OptoDesigner Phoenix SoftwareTM the solution was analysed and optimized. Some comparisons are drawn between this solution and the other Magic-T previous analysed. Lastly an Haar Network is also implemented with the designed Magic-T and simulated with OptoDesigner, concluding that it is a viable solution with a good power performance and a possible substitute to some devices already implemented with other Magic-T. This device will be implemented in the project COMPRESS, with the aim to replace a coupler that also reproduces the Haar Transform.

Contents

Contents	i
List of Figures	v
List of Tables	vii
Acronyms	ix
1 Introduction	1
1.1 Context and Motivation	1
1.2 Objectives	4
1.3 Structure Overview	4
1.4 Contributions	5
2 Multimode Interferometer Self-Imaging Model	7
2.1 Multimode Waveguide	7
2.1.1 Propagation Constants	8
2.1.2 Guided Mode Propagation	10
2.2 General Interference	13
2.2.1 Single Images	13
2.2.2 Multiple Images	14
2.3 Restricted Interference	17
2.3.1 Paired Interference	17
2.3.2 Symmetric Interference	19
2.4 Multimode Interferometer characteristics	20

2.4.1	Proprieties and Requirements	20
2.4.2	Imaging Quality	21
2.4.3	Reflecting Properties	22
3	Multimode Interferometer architectures	23
3.1	Architectures Introduction	23
3.2	Tapered Multimode Interferometer	24
3.2.1	Linear Tapered Multimode Interferometer	24
3.2.2	Parabolic and Exponential Tapered Multimode Interferometer	25
3.3	Butterfly Multimode Interferometer	27
3.3.1	Tapered Butterfly Multimode Interferometer	27
3.3.2	Parabolic Butterfly Multimode Interferometer	28
4	Haar Transformation	31
4.1	Introduction	31
4.2	Theoretical implementation of the Haar Wavelet Transform	32
4.3	Haar transform - image processing and compression	34
4.4	Optical Haar Transform Network Implementation	36
4.5	3-dB Asymmetric Haar Coupler Design	37
5	Magic-T exploratory analysis	41
5.1	8 x 8 Multimode Interferometer Coupler Magic-T	41
5.2	2 x 3 Multimode Interferometer Coupler Magic-T	43
5.3	Multimode Interferometer couplers with arbitrary power coupling ratios	46
6	Projecting novel architectures for Haar Wavelet Transform	49
6.1	Foundry introduction	49
6.2	2 x 3 Multimode Interferometer Coupler	51
6.3	2 x 2 Linear Multimode Interferometer	55
6.4	2 x 2 Tapered Butterfly Multimode Interferometer	61
6.5	2 x 2 Parabolic Butterfly Multimode Interferometer	64
6.6	Final design optimization	67
6.7	Haar Network Implementation	70

7 Conclusion and Future work	73
Bibliography	75
A MMI 2 x 2 with access waveguide length change	79
B Future work MMI architecture	81

List of Figures

1.1	Schematic of different area branches that are forming part of integrated photonics	3
2.1	N x M Multimode Interefometer Structure	8
2.2	Two-dimensional representation of a step-index multimode waveguide and the effective index profile, and top view of multimode waveguide with the coordinate system [1]	8
2.3	Guided modes in a step-index multimode waveguide	9
2.4	Input field and mirrored images through the length of the multimode section [1]	11
3.1	Linear-tapered MMI [2]	24
3.2	Parabolic and Exponential Tapered MMI [3]	26
3.3	Geometrical design of the Besse butterfly MMI [4]	27
3.4	David Levy Parabolic Tapered MMI [5]	28
4.1	Process of a signal decomposition using multi-resolution analysis	32
4.2	Band decomposition using wavelet transform	33
4.3	System building blocks for Haar optical wavelet transform based on image processing and compression [6]	35
4.4	3D basic module for the first level optical 2D Haar Transform [6]	37
4.5	Schematic of the 3-dB asymmetric coupler [7]	38
5.1	Schematic diagram of El-Sabban et al. MMI structure designed to perform the Magic-T functions [8]	44
5.2	Optical distribution in the MMI structure for in-phase (left) and out-of-phase (right) excitation [8]	45

5.3	Redrawn graphic from the frequency response of the MMI device [8]	46
6.1	El-Sabban [8] 2 x 3 MMI design adaptation	51
6.2	Haar Network schematic	53
6.3	2 x 3 MMI with a phase shifter	53
6.4	Phase shifter waveguide design	56
6.5	Linear MMI Schematic	57
6.6	Power propagation along the 2 x 2 MMI with separated input signals	58
6.7	Power propagation along the 2 x 2 MMI	59
6.8	Linear MMI Insertion Loss	59
6.9	Linear MMI phase performance	60
6.10	Overall Linear MMI Insertion Loss	60
6.11	MMI Tapered Butterfly Schematic	61
6.12	Power propagation along the 2 x 2 Tapered Butterfly MMI	62
6.13	Tapered Butterfly MMI Insertion Loss	63
6.14	Tapered Butterfly MMI phase performance	63
6.15	Overall Tapered Butterfly MMI Insertion Loss	64
6.16	MMI Parabolic Butterfly Schematic	65
6.17	Power propagation along the 2 x 2 Parabolic Butterfly MMI	65
6.18	Parabolic Butterfly MMI Insertion Loss	66
6.19	Parabolic Butterfly MMI phase performance	67
6.20	Overall Parabolic Butterfly MMI Insertion Loss	67
6.21	Position sweep for width reduction position	68
6.22	Magic-T output phase with 180° extra input phase	69
6.23	MMI Haar Network	70
6.24	BPM simulation on the Haar Network	70
A.1	Linear MMI Insertion Loss	79
A.2	Linear MMI phase performance	80
A.3	Overall Insertion Loss in C-band range	80
B.1	Prototype MMI architecture design	81
B.2	Prototype design BPM simulation	82

List of Tables

2.1	Summary of characteristics of the general, paired and symmetric interference mechanisms [1]	20
4.1	Output values from the simulated 3-dB asymmetric coupler [7]	38
5.1	Phase difference between the 8 x 8 MMI ports [9]	42
5.2	8 x 8 MMI coupler output power measures[9]	43
5.3	Phase difference between 2 x 2 MMI	47
5.4	Phase difference required for the Magic-T	48
6.1	Phase and Overlap relations for both inputs working separately	52
6.2	2 x 3 MMI output signals	52
6.3	Phase and Overlap relations for both inputs working separately	54
6.4	2 x 3 MMI output power signal as input sums	54
6.5	Phase difference required for the Magic-T	55
6.6	Waveguide parameters value	56
6.7	Output power and phase	58
6.8	Tapered Butterfly output phase and power	62
6.9	Parabolic Butterfly output phase and power	66
6.10	Insertion loss of each MMI and main parameters	68
6.11	Optimized MMI output phase and power	69
6.12	Haar Network output phase and power	71

Acronyms

MMI	Multimode Interferometer
PICs	Photonic Integrated Circuits
1D	One-Dimensional
2D	Two-Dimensional
3D	Three-Dimensional
BPM	Beam Propagation Method
WT	Wavelet Transforms
EM	Electromagnetic
DWT	Discrete Wavelet Transform
HWT	Haar Wavelet Transform
LP	Low-Pass
MM	Multimode
IL	Insertion Loss
HP	High-Pass
IR	Infrared
UV-B	Ultraviolet-B
SOI	Silicon on Insulator

PDK	Process Design Kit
BB	Building Blocks
FhG-HHI	Fraunhofer-Gesellschaft Heinrich-Hertz Institute
COBRA	Communication technologies; Basic Research and Applications
InP	Indium Phosphide
JePPIX	Joint European Platform for Photonic Integration of Components and Circuits
CMOS	complementary metal–oxide–semiconductor
CMT	Coupled Mode Theory

Chapter 1

Introduction

1.1 Context and Motivation

Technological evolution is part of mankind since the beginning and it has been growing and expanding even more nowadays, simplifying our way of living. With the evolution of telecommunication networks on flexibility and reconfigurability, the use of optical circuits is growing.

Optics are defined as a section of physics which studies the generation and propagation of light and its interaction with matter. Essentially, light is the main subject of optics and it is defined as Electromagnetic (EM) radiation. In the optical wavelength, the window can be extended from the vacuum Ultraviolet-B (UV-B), at about 300 nanometers, to the far Infrared (IR) at 700 nanometers [10]. The invention of the laser by Theodore Harold Maiman [11] allowed the opportunity of coherent light sources with notable proprieties. With the development of semiconductor optical devices, for generation and detection of light, there was a revolution in modern optics. As a result of this revolution, new fabrication techniques emerged. This events granted very efficient, compact and cheap devices with low propagation losses.

This transformation in the field of optics associated with other technologies caused the appearance of new fields such as electro-optics, quantum electronics, waveguide technology, etc. These new areas describe a new range and diversity of more complex devices for instance

lasers, semiconductor detectors, light modulators, etc. The operation of these devices, in terms of electronics and optics, originated the field of photonics.

Photonics emphasizes the role that electronics plays in optical devices and also the necessity of treating light in terms of photons rather than waves, particularly in terms of matter-light interactions [10]. The emerging of new photonic devices resulting from the electronics and optics connection, has created new sub-areas within photonics, being integrated photonics one of this branches.

The term - integrated photonics - refers to the fabrication and integration of several photonics components on a common planar substrate. These components include beam splitters, gratings, couplers, polarisers, interferometers, sources and detectors, among others. It is possible to fabricate, using these components as building blocks, more complex devices that can work in a wider range of functions with applications in community access television, sensors and optical communications systems.

Photonic Integrated Circuits (PICs) are being more and more commercialized due to their less power consumption, lower cost and easier assembly of numerous and complex systems, smaller volume and weight and higher thermal and mechanical stability. The assemble of integrated photonic technology can be considered as the convergence of different photonics' areas of study with waveguide technology.

The basic element in integrated photonic technology is the optical waveguide. One can defined a waveguide as an optical structure that allows, by total internal reflection, the confinement of light within its boundaries. Optical waveguides are, therefore, the key element of PICs. Waveguides can perform multiplexing and demultiplexing, coupling, switching and splitting of optical signals. Briefly, integrated photonics is constituted by combining waveguide technology with other areas of optics, as shown in figure 1.1.

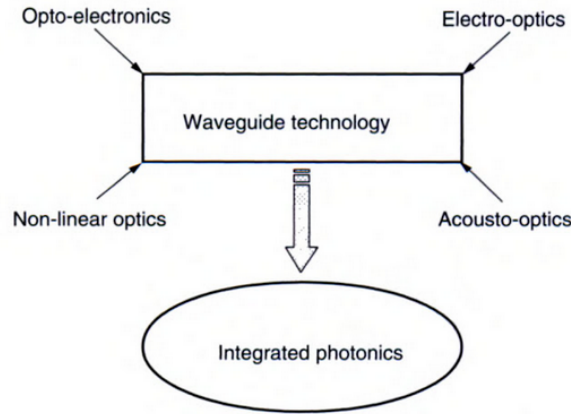


Figure 1.1: Schematic of different area branches that are forming part of integrated photonics

Waveguides are used as components or as constituents of components in integrated optical circuits. One of those components is the Multimode Interferometer (MMI). The interest in the application of MMI devices is spreading in recent years due to their good proprieties and characteristics that fulfilled PICs factors for commercialization. Their excellent properties have led to their rapid incorporation in more advance and complex PICs devices such as MachZehnder switches and modulators, balanced coherent receivers, ring lasers and optical hybrids for phase diversity networks [1].

MMI devices are a multimode waveguide that distributes optical power from N inputs to M outputs, both integers. It is based on constructive and destructive interferences phenomena occurring in the Multimode (MM) area. These devices use the self-imaging principle in order to obtain multiple images of the input field profile over the length [12].

The main focus of this thesis is to develop an optical tool that implements layers of optical compression, applicable to any type of signal, to be integrated in the FCT COMPRESS project. The solution applied is the Magic-T. It is a coupler that does additions and subtractions in the optical domain which allows to implement the Haar Wavelet Transform (HWT).

In this digital era the computer and video-media have been evolving and growing. The image compressing methods must keep up this growth in order to fulfil the high performance,

speedy digital videos and audio capabilities requirements. The HWT is a Discrete Wavelet Transform (DWT) that offers simplicity and fast computation.

Despite the fact that the Magic-T has already been implemented with a coupler [7] and with an 8 x 8 MMI in the same project this thesis is inserted, the operation with a 2 x 2 MMI is the main achievement for this study. With this accomplishment, the MMI will have 1/10 of the coupler size, which means having a length around the $300\mu m$. It can succeed the development of more complex transforms and consequently more useful for real systems in a level of compression, signal input number or points simultaneous processed by one optical chip.

1.2 Objectives

In order to achieve a 2 x 2 MMI magic-T, it will be necessary to go through the following objectives:

- Study the MMI parameters and behaviour;
- Understand the HWT;
- Study of all-optical image processing system;
- Analysis on available foundries for the MMI;
- Design the MMI for a specific foundry;
- Simulate the MMI solution and optimize it for the proprieties needed;
- Implement the MMI on an Haar network;

1.3 Structure Overview

This project is structured in the following way:

- **Chapter 2: Multimode Interferometer Self-Imaging Model.** This chapter will point to the mathematical approach to self-imaging principle and the phenomena that

occurs in the central MMI waveguide. A complete study is presented with equations on all the main aspects of a linear MMI;

- **Chapter 3: MMI architectures.** The third chapter refers different possible designs of MMI and the differences relatively to the linear one. It also points out the advantages of each type comparatively to each other for a better design of MMI;
- **Chapter 4: Haar Transformation.** In this chapter the Haar Wavelet Transform is analysed with a focus on the main characteristics, proprieties and advantages towards other transforms, in order to study image processing. Regarding this compression method, a solution of an all-optical architecture is also analysed;
- **Chapter 5: Magic-T exploratory analysis.** Along this chapter, an analyse on all the implementations of the Magic-T is formed. The essential ideas of each architecture are focused in order to understand their strengths and weaknesses;
- **Chapter 6: Projecting novel architectures for Haar Wavelet Transform.** A succinct introduction to the foundry used is done in this section. The design and implementation of the architectures are made using OptoDesigner Phoenix SoftwareTM. There are two presented solutions, where the first solution was adapted from literature and the other, as an adaptation of various designs, was achieved through simulations. The final solution is implemented and simulated as an Haar Network;
- **Chapter 7: Conclusions and Future work.** The last chapter focus on the work done through this thesis and the main conclusions and achievements. Also it includes a proposal of a possible design to be develop with a tilted MMI.

1.4 Contributions

The main contributions are the follow:

- Design of an 2x2 MMI for a specific foundry that performs the HWT;
- Simulation of an adapted and new solution for the HWT;
- New solution for the second order HWT, for the FCT COMPRESS project;

- Paper submission to the *III International Conference on Applications in Optics and Photonics* "Haar Wavelet Transform with a 2 x 2 MMI" - João Fernandes, Francisco Rodrigues, Mário Lima and António Teixeira.

Chapter 2

Multimode Interferometer Self-Imaging Model

In December 1836, Talbot described the first self-imaging of periodic objects illuminated by coherent light [13]. The MMI behaviour is based on this self-imaging principle. The principle consists on producing single or multiple images of the input optical field at periodical intervals along the propagation waveguide. It was first suggested by Bryngdahl [14] and explained in more detail by Ulrich [15, 16] the possibility of reaching self-imaging in uniform index slab waveguide. In order to simplify references, this chapter is based on Soldano et al. [1] and presents an overview of integrated optics based on MMI. It also refers the MMI superior performance when compared to alternatives such as couplers or junctions.

2.1 Multimode Waveguide

The MMI device can be divided in two main blocks. The first block is the central section waveguide, which is a MM section that is excited by the input segments and is able to propagate more than three modes. The other block is composed by the access waveguides, inputs and outputs waveguides. Inputs launch light into the main section and the outputs recover the light from it. Both access waveguides usually propagate singlemode for the high-performance of the MMI device.

This devices are described as $N \times M$ MMI, where N and M are the number of input and

output waveguides respectively, as observed at figure 2.1.



Figure 2.1: $N \times M$ Multimode Interferometer Structure

The best approach to understand the self-imaging phenomenon is a full-modal propagation analysis. Before considering imaging along different shape structures, it is useful to know how to scale out the parameters on a linear MMI.

2.1.1 Propagation Constants

The MM section is composed by a step-index waveguide with width W_M , ridge refractive index n_r and cladding refractive index n_c , as shown in the figure 2.2.

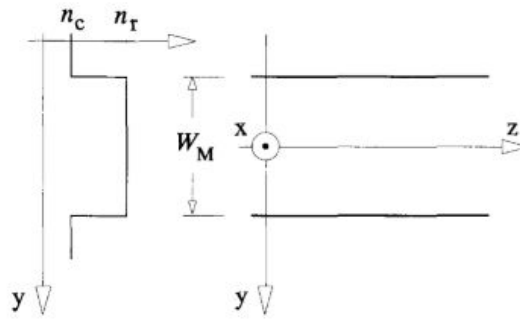


Figure 2.2: Two-dimensional representation of a step-index multimode waveguide and the effective index profile (left), and top view of multimode waveguide with the coordinate system (right) [1]

The MM waveguide at a free-space wavelength λ_0 supports m lateral modes with mode

numbers $v = 0, 1, 2, \dots(m - 1)$, as showed in figure 2.4.

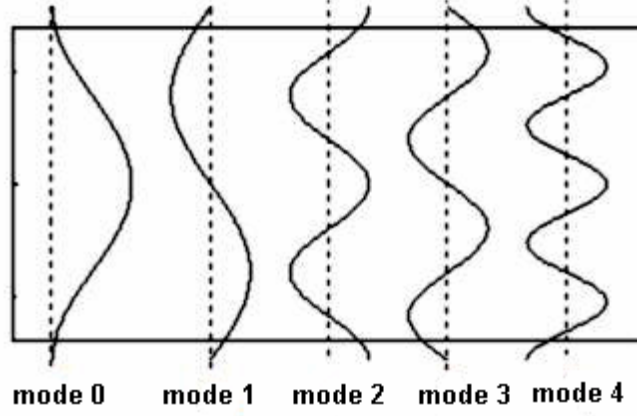


Figure 2.3: Guided modes in a step-index multimode waveguide

The follow equation can relate the lateral wavenumber k_{yv} and the propagation constant β_v to the ridge index n_r

$$k_{yv}^2 + \beta_v^2 = k_0^2 n_r^2 \quad (2.1)$$

with

$$k_0 = \frac{2\pi}{\lambda_0}, \quad (2.2)$$

$$k_{yv} = \frac{(v+1)\pi}{W_{ev}}. \quad (2.3)$$

The effective width, W_{ev} , takes into consideration the lateral penetration depth of each mode field, and for high-contrast waveguides, this width can be approximated to W_M , since the penetration depth is very small. Generally the effective index is approximated by the fundamental mode $v = 0$ width, W_{e0} as presented below in equation 2.4,

$$W_{ev} \simeq W_{e0} = W_M + \left(\frac{\lambda_0}{\pi}\right) \left(\frac{n_c}{n_r}\right)^{2\sigma} (n_r^2 - n_c^2)^{-(1/2)} \quad (2.4)$$

where $\sigma = 0$ is for TE and $\sigma = 1$ is for TM polarization. One can then deduce the propagation constant β_v from equations 2.1, 2.2 and 2.3.

$$\beta_v \simeq k_0 n_r - \frac{(v+1)^2 \pi \lambda_0}{4 n_r W_{e0}^2}. \quad (2.5)$$

Defining L_π as the beat length of the two lowest-order modes

$$L_\pi = \frac{\pi}{\beta_0 - \beta_1} \simeq \frac{4 n_r W_{e0}^2}{3 \lambda_0} \quad (2.6)$$

and using the propagation constant equation a relation between propagation constants spacing was establish as follows

$$(\beta_0 - \beta_v) \simeq \frac{v(v+2)\pi}{3L_\pi}. \quad (2.7)$$

2.1.2 Guided Mode Propagation

It is possible to decompose the input field profile, $\Psi(y, 0)$ at $z = 0$, into the modal field distributions of all guided and radiative modes $\Psi_v(y)$ as presented below,

$$\Psi(y, 0) = \sum_v c_v \psi_v(y) \quad (2.8)$$

and also shown in figure 2.4.

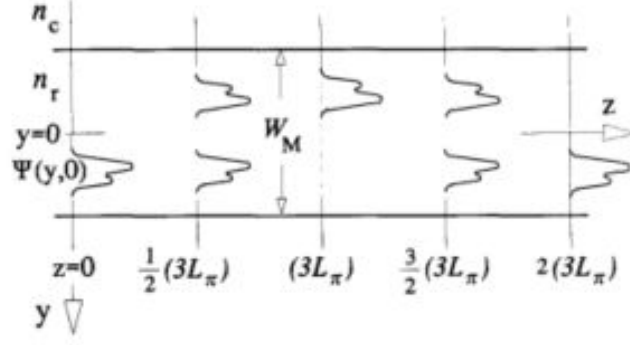


Figure 2.4: Input field and mirrored images through the length of the multimode section [1]

Based on the field-orthogonality relation and using overlap integrals, the field excitation coefficients c_v can be estimated

$$c_v = \frac{\int \psi_v(y, 0) \psi_v(y) dy}{\sqrt{\int \psi_v^2(y) dy}}. \quad (2.9)$$

One can decompose the guides modes alone if the spectrum of the input field $\Psi(y, 0)$ is sufficiently narrow to not excite unguided modes

$$\Psi(y, 0) = \sum_{v=0}^{m-1} c_v \psi_v(y). \quad (2.10)$$

At a distance z it is possible to write the field profile as

$$\Psi(y, z) = \sum_{v=0}^{m-1} c_v \psi_v(y) \exp[j(\omega t - \beta_v z)]. \quad (2.11)$$

This field is an algebraic sum of all guided mode field distributions.

Using the phase of fundamental mode as a common factor out of the sum, dropping it and assuming the time dependence, $\exp(j\omega t)$, implicit hereafter, the field $\Psi(y, z)$ results in

$$\Psi(y, z) = \sum_{v=0}^{m-1} c_v \psi_v(y) \exp[j(\beta_0 - \beta_v)z] \quad (2.12)$$

The expression for $z = L$ is obtained by using the equation above and substituting equation 2.7 in it

$$\psi(y, L) = \sum_{v=0}^{m-1} c_v \psi_v(y) \exp[j \frac{v(v+2)\pi}{3L_\pi} L]. \quad (2.13)$$

The modal excitation c_v and the proprieties of the mode phase factor

$$\exp[j \frac{v(v+2)\pi}{3L_\pi} L] \quad (2.14)$$

will determine the types of images formed and the aspect of $\Psi(y, L)$.

It can be detected that, in some situations, the field $\Psi(y, L)$ will be a duplicate of the input field $\Psi(y, 0)$. To the self-imaging mechanisms which are independent of the modal excitation it is called General Interference, and to those obtained through exciting certain modes alone it is called Restricted Interference.

2.2 General Interference

This section addresses the interference mechanisms independent of the modal excitation, with no restriction on the coefficients c_v . It also explores the periodicity of the mode phase factor, equation 2.14.

2.2.1 Single Images

One can verify with equation 2.13 that $\Psi(y, L)$ will be a reply image of $\psi(y, 0)$ if

$$\exp[j\frac{v(v+2)\pi}{3L_\pi}L] = 1 \text{ or } (-1)^v. \quad (2.15)$$

The meaning of the first condition is that the phase changes of all the propagation modes along the length L must differ by integer multiples of 2π . All the guided modes, in this case, interfere with the same relative phases as in the reference source $z = 0$. The image is therefore a replica of the input field. The second condition implies that the phase changes must be alternatively even and odd multiples of π .

$$\psi_v(-y) = \begin{cases} \psi_v(y) & \text{for } v \text{ even} \\ -\psi_v(y) & \text{for } v \text{ odd} \end{cases} \quad (2.16)$$

The even modes will be in phase and the odd modes in a difference in phase of 180° . Due to the odd symmetry exposed in piecewise equation 2.16, the image caused by the interference will be mirrored relatively to $y = 0$.

$$v(v+2) = \begin{cases} \text{even} & \text{for } v \text{ even} \\ \text{odd} & \text{for } v \text{ odd} \end{cases} \quad (2.17)$$

Taking the equivalence from equation 2.17 into consideration, it is visible that both conditions for equation 2.15 will be fulfilled at

$$L = p(3L_\pi) \text{ with } p = 0, 1, 2, \dots \quad (2.18)$$

with p even for the first condition and p odd for the second condition. The factor p stands for the periodic nature of the imaging along the multimode waveguide. Direct and mirrored single images of the input field $\Psi(y, 0)$ will consequently be formed by general interference at the even and odd multiplies distances, respectively, of the length $(3L_\pi)$, as observed in figure 2.4.

2.2.2 Multiple Images

The multiple imaging phenomenon provides the basis for a broader range of MMI couplers. In addition to the single images at distances z given by equation 2.18, it is also possible to find multiples images as well at halfway distance between direct and mirrored images

$$L = \frac{p}{2}(3L_\pi) \quad (2.19)$$

where in this case, p has to be a odd number, $p = 1, 3, 5, \dots$

The total field is found by substituting equation 2.13 into 2.19 at these given lengths

$$\Psi(y, \frac{p}{2}3L_\pi) = \sum_{v=0}^{m-1} c_v \psi_v(y) \exp[jv(v+2)p(\frac{\pi}{2})] \quad (2.20)$$

where p is an odd integer. With the properties of equation 2.17 and the mode field symmetry

conditions of 2.16, the total field can be written as

$$\begin{aligned}\Psi(y, \frac{p}{2}3L_\pi) &= \sum_{v \text{ even}} c_v \Psi_v(y) + \sum_{v \text{ odd}} (-j)^p c_v \Psi_v(y) \\ &= \frac{1 + (-j)^p}{2} \Psi(y, 0) + \frac{1 - (-j)^p}{2} \Psi(-y, 0)\end{aligned}\tag{2.21}$$

This equation shows a pair of images of $\Psi(y, 0)$ with $1/\sqrt{2}$ of amplitude and in quadrature, at distances $z = \frac{1}{2}(3L_\pi), \frac{3}{2}(3L_\pi), \dots$, as observed in figure 2.4. It is possible to implement 2 x 2 3-dB couplers with this two fold imaging.

Normally, multi-fold images are formed at intermediate z-positions. Through Fourier analysis and proprieties of generalized Gaussian sums, Soldano et al. [1] obtained analytical expressions for the positions and phases of the N-fold images as shown in equation 2.22. To start this analysis, a field $\Psi_{in}(y)$ is introduced as an extension of the input field $\Psi(y, 0)$, asymmetric with the plane $y=0$ and with periodicity of twice the effective width W_e

$$\Psi_{in}(y) = \sum_{v=-\inf}^{\inf} [\Psi(y - v2W_e, 0) - \Psi(-y + v2W_e, 0)].\tag{2.22}$$

The mode field amplitudes can be approximated to a sine-line function

$$\psi_{in}(y) \simeq \sin(k_{yv}y)\tag{2.23}$$

allowing the possibility to consider it as a Fourier expansion at distances

$$L = \frac{p}{N}(3L_\pi)\tag{2.24}$$

where $p \geq 0$ and $N \geq 1$ are integers with no common divisors, and the field will be expressed as

$$\Psi(y, L) = \frac{1}{C} \sum_{q=0}^{N-1} \Psi_{in}(y - y_q) \exp(j\varphi_q) \quad (2.25)$$

with

$$y_q = p(2q - N) \frac{W_e}{N} \quad (2.26)$$

$$\varphi_q = p(N - q) \frac{q\pi}{N} \quad (2.27)$$

where C is a complex normalized constant with $|C| = \sqrt{N}$, p refers to the imaging periodicity along direction z and q represents each of the N images along y direction. These equations show that, at distances $z = L$, N images are formed of the extended field $\Psi_{in}(y)$ located at the position y_q , each with $1/\sqrt{N}$ and phase φ_q . This points to N images, normally not equally spaced between them, of the input field, being formed inside the physical guide and within the lateral boundaries.

It is possible to accomplish $N \times N$ or $N \times M$ optical couplers due to the multiple self-imaging mechanism. Shorter devices are obtained with $p = 1$ and their optical phases for a $N \times N$ coupler are

$$\varphi_{rs} = \frac{\pi}{4N} (s - 1)(2N + r - s) + \pi \quad \text{for } r + s \text{ even} \quad (2.28)$$

and

$$\varphi_{rs} = \frac{\pi}{4N}(r+s-1)(2N-r-s+1) + \pi \text{ for } r+s \text{ odd} \quad (2.29)$$

where $r = 1, 2, \dots, N$ is the numbering of the input waveguide and $s = 1, 2, \dots, N$ is the numbering of the output waveguides. The count is done bottom-up and top-down, respectively.

The phase relation given from both equations is inherent to the image proprieties of multimode waveguide.

2.3 Restricted Interference

Until this section, no restrictions have been place on the modal excitation. MMI couplers allow this restrictions on the modal excitation. This means that not all the guided modes in the MM waveguide are excited by the input fields. This selective excitation reveals interesting multiplicities of $v(v+2)$ which makes new interference mechanisms possible through shorter periodicities of the mode phase factor.

2.3.1 Paired Interference

The length periodicity of the mode phase factor of equation 2.14 can be reduced to a third of the the original size

$$\text{mod}_3[v(v+2)] = 0 \text{ for } v \neq 2, 5, 8, \dots \quad (2.30)$$

But in order to verify this, the following condition must be taken into account

$$c_v = 0 \text{ for } v = 2, 5, 8, \dots \quad (2.31)$$

Single direct and inverted images of the input field $\Psi(y, 0)$ can be now obtained at

$$L = p(L_\pi) \text{ with } p = 0, 1, 2, \dots \quad (2.32)$$

as long as the modes $v = 2, 5, 8, \dots$ are not excited in the multimode waveguide. The two-fold images are found at $(p/2)L_\pi$ with p odd. N-fold images based on numerical simulations will be formed at the distance

$$L = \frac{p}{N}(L_\pi) \quad (2.33)$$

where $p \geq 0$ and $N \geq 1$ are integers with no common divisor.

One way of obtaining the selective condition of excitation, equation 2.31, is by launching an even symmetric input field, usually a Gaussian beam, at $y = \pm W_e/6$. The modes $v = 2, 5, 8, \dots$ have a zero with odd symmetry. The overlap integrals of the field excitation coefficient c_v between the symmetric input and the asymmetric mode fields will disappear and consequently obtaining $c_v = 0$ for $v = 2, 5, 8, \dots$. In this particular case, the number of input waveguides is limited to two.

When the selective excitation condition is satisfied, the modes contributing to the imaging are paired, in other words the mode pairs 0-1, 3-4, 6-7, ... will have similar properties and based on this fact, they obtain the termination of paired interference. Each even mode leads its odd partner by a phase difference of $\pi/2$ at $z = L_\pi/2$ and by a phase difference of π at $z = L$.

2.3.2 Symmetric Interference

Optical 1 x N splitters can be achieved on the basis of the general N-fold imaging at the lengths of equation 2.24. However 1 x N beam splitters, in which the modes excited are only the even symmetric modes, can be accomplish four times shorter with MM waveguides

$$\text{mod}_4[v(v+2)] = 0 \text{ for } v \text{ even} \quad (2.34)$$

In the equation above, one can verify that the length periodicity of the mode phase will be reduced if

$$c_v = 0 \text{ for } v = 2, 5, 8, \dots \quad (2.35)$$

Consequently the direct and inverted single images of the input field $\Psi(y, 0)$ can be accessed at the length of

$$L = p\left(\frac{3L_\pi}{4}\right) \text{ with } p = 0, 1, 2, \dots \quad (2.36)$$

if the odd modes are not excited in the MM waveguide. One can obtain this condition, with a symmetric field profile, by centre-feeding the multimode waveguide. The mechanism of obtaining the imaging through linear combinations of even symmetric modes it was named as symmetric interference. It is possible to achieve N images of the input field, symmetrically located along the y-axis, with W_e/N spacing at distances

$$L = \frac{p}{N}\left(\frac{3L_\pi}{4}\right). \quad (2.37)$$

2.4 Multimode Interferometer characteristics

MMI devices have some differences when compared to other couplers and routing devices. The table 2.1 compiles the main proprieties of the general, paired and symmetric interference mechanisms.

Table 2.1: Summary of characteristics of the general, paired and symmetric interference mechanisms [1]

Interference mechanism	General	Paired	Symmetric
Inputs x Outputs	N x N	2 x N	1 x N
First single image distance	$(3 L_\pi)$	(L_π)	$(3L_\pi)/4$
First N-fold image distance	$(3L_\pi)/N$	$(L_\pi)/N$	$(3L_\pi)/4N$
Excitation requirements	none	$c_v = 0$ for $v = 2, 5, 8...$	$c_v = 0$ for $v = 1, 3, 5...$
Input(s) location(s)	any	$y = \pm We/6$	$y = 0$

This section examines the way self-imaging affects and change the design and behaviour characteristics of the MMI.

2.4.1 Proprieties and Requirements

The general interference mechanism is conventionally independent of the position and shape of the input waveguide fields. Nonetheless, by simulation and experimental modes, it is possible to verify that the MMI performance can be optimized when changing the position of the access waveguides.

The restricted interference mechanisms must have the input fields in a well displayed and located symmetry concerning the selective modal excitation requirements for both paired con-

dition 2.31 and symmetric condition 2.35.

When discussing the case of 2 x 2 couplers, the paired interference points to longer devices when compared to general interference mechanism. There is an increase in the MM waveguide width and length, as a result of the selective excitation requirement. As a consequence of it, there is a cancellation of the length reduction potential. However, when referring to weakly guiding structures, equation 2.14, the paired interference mechanism has fewer losses than the general interference as an effect of the decreased image resolution, which is described in the next subsection.

2.4.2 Imaging Quality

The quality of the image indicates how accurate the input field is reproduced at the end of the MM section.

The guided modes will accumulate some deviations from the calculated phases at the image distances as a result of the approximation of the quadratic dependence of the propagation constants with mode number 2.5. This tends to blur the reconstructed imaged field.

The imaging resolution is an advantageous parameter when designing an MMI coupler. When an input field is launched from the access waveguide the MM waveguide must be capable of providing an image field as narrow of the same input. For a - W_e - width of the MM waveguide, the resolution p is calculated by the number of guided modes m that can be propagated in the same MM section.

$$p \approx \frac{W_e}{m} [1] \quad (2.38)$$

The number of guided modes can be determined by the lateral refractive index contrast in ridge waveguides.

2.4.3 Reflecting Properties

Distinct applications such as lasers and coherent detection techniques are very sensitive to reflections. Reflections in the MMI can be created at the end of the waveguide between the output guides.

There are some situations where reflection may occur, as an example, when large refractive index differences come across. When the length is not optimized, some light can reflect at end of the MMI and reaching the input guides. But even when the length is optimized it occurs reflection. In this situation, the reflection can be very effective because the mechanisms involve the same imaging proprieties of the MM waveguides.

There are two identified reflection mechanisms. The first is an internal resonance which is caused by the presence of several simultaneously occurring self-images. As an example, a 3 dB MMI is based on the two fold image at the length of $3L_\pi/2$, as mentioned in equation 2.19. This length is twice the self imaging size for symmetric excitation, $L = 3L_\pi/4$, given by equation 2.36. This symmetric self-imaging mechanism ensures efficient imaging of both reflecting ends into each other. General and symmetric self-imaging occurring at the same time can be prevented by using couplers based on paired interference. The second reflection mechanism can be found when using an MMI power splitter in reverse as a power combiner. In this case the two inputs are 180° out of phase, which causes the power to be minimum in one of the output guides and maximum at the reflecting end of the MM section. This points to perfect imaging of the input guides back towards themselves. For a single MMI combiner optimized for maximum transmission back, reflection can differ from a minimum in-phase excitation to a maximum out-of-phase excitation.

Chapter 3

Multimode Interferometer architectures

This chapter explains the different MMI designs and its main characteristics at the MM waveguide. This study intends, through the use of analytical analysis methods, to choose the design that suits better as a solution for reducing the MMI length and width. Consequently this will improve the future Magic-T solution.

3.1 Architectures Introduction

Lately, large $N \times N$ MMI structures, with $N \geq 4$, have been used as splitting and recombining elements. The number of ports and the nature of self-imaging principle, which these structures have been utilized, requires that these devices must be on the order of several millimetres in length [17]. The more one increases the number of ports, the more it has to increase the MMI region width, which also increases the length by a ratio of width square, as observed on equation 2.6, causing the length to scale normally to centimeters. This large length makes it difficult to implement it on useful system applications.

The obstacles created by the size of the MMI based devices led to the importance of making them with the smallest possible dimensions. The most important action to minimize the device size is to diminish the width by ensuring the input and output waveguides are placed

in the closest allowable proximity while using only one type of imaging, general or restricted. However there is also the possibility of reducing the size of the device by applying a taper on the MM region. The next sections focus on different tapered MMI already reported and its characteristic towards the decrease of the device length.

3.2 Tapered Multimode Interferometer

3.2.1 Linear Tapered Multimode Interferometer

Seok-Hwan Jeong and Ken Morito reported in 2010 [2] and 2011 [3] a compact optical 90° hybrid employing a tapered 2 x 4 MMI coupler serially connected by a 2 x 2 MMI coupler. In specific, the tapered shape MMI analysis describes its behaviour and advantages in comparison to a linear MMI.

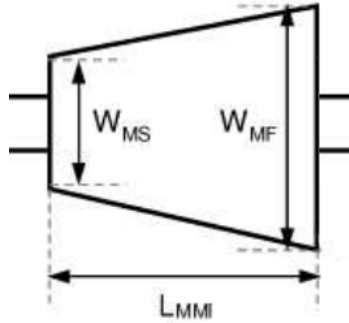


Figure 3.1: Linear-tapered MMI [2]

The shape of the tapered is a simple trapezoid, with W_{MS} as the small base and W_{MF} as the big base, so it is easy to characterize its modulation function as

$$W_M(z) = W_{MS} + (W_{MF} - W_{MS}) \frac{z}{L_{mmi}} [2] \quad (3.1)$$

where L_{MMI} represents the length of the linear-tapered MMI coupler and z the position over

it length. The two lowest-order modes is given by

$$(\beta_0 - \beta_v) \simeq \frac{v(v+2)\pi\lambda}{4N_{eq}W_{MF}^2}\chi^T[2]. \quad (3.2)$$

where χ^T is a proportional constant that creates a relation between both MM section widths. It can be defined as

$$\chi^T = \frac{W_{MF}}{W_{MS}}[2]. \quad (3.3)$$

Relating both above equations 3.2 and 3.3, it is possible to define the lowest order modes beat length of the linear-tapered MMI coupler as

$$L_\pi^T = \frac{4n_r W_{MF}^2}{3\lambda} \frac{1}{\chi^T} \quad (3.4)$$

As observed the MMI length can be reduced by a proportion of χ^T . All above equations are approximations validated under the condition that all the effective MMI widths, for each excited mode at the MMI region, are identical and each propagation constant, β_v , is treated as the Taylor series [2].

The image formation conditions in this type of MMI are different from the linear one as a result of the the phase difference between modes along the tapered field changes with it shape.

3.2.2 Parabolic and Exponential Tapered Multimode Interferometer

Jeong et al. also reported a Parabolic and Exponential Tapered MMI [3] as observed in figure 3.2. The curvature is the different between both tapered, as each one has a different

characterization equation.

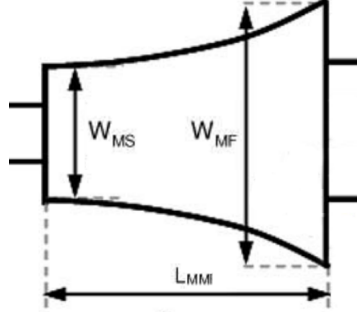


Figure 3.2: Parabolic and Exponential Tapered MMI [3]

The equations for the Parabolic and and Exponential Tapered modulation function are, respectively

$$W_{MP}(z) = W_{MS} + (W_{MF} - W_{MS})\left(\frac{z}{L_{mmi}}\right)^2 [3] \quad (3.5)$$

$$W_{ME}(z) = W_{MS} + (W_{MF} - W_{MS})\left(\frac{\text{Exp}(z/L_{MMI}) - 1}{e - 1}\right) [3] \quad (3.6)$$

Both cases can reduce the length by a ratio of χ^T , equation 3.3.

These types of tapered shapes are better to apply in $N \times M$ MMI as Jeong did, where $M > N$. The input side of the MM section, since it has less width, does not allow to have as much access waveguides as the output side.

For the reduction of size to be efficient in a $N \times N$ MMI, the tapered needs to be applied in the middle of the MM waveguide and not in the beginning. In this type of architectures the maximum width reduction can be only achieved by reducing the gap, between input and output ports, to the minimum possible size.

3.3 Butterfly Multimode Interferometer

3.3.1 Tapered Butterfly Multimode Interferometer

Power splitting is a basic function of the PICs and various solutions have been proposed and realized in the past years using MMI. Using the MMI standard design one can only obtain discrete values of splitting ratios when an overlapping of self images is introduced. Pierre A. Besse et al. [4] reported different formats of MMI for a free selection of power splitting ratios.

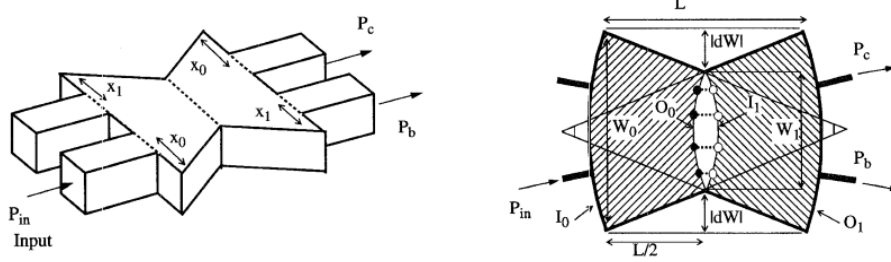


Figure 3.3: Geometrical design of the Besse butterfly MMI [4]

The MMI length is expressed by

$$L_\pi \cong \frac{4n_r(W_0W_1)}{3\lambda} [4] \quad (3.7)$$

where W_1 and W_0 are the widths at the centre and at the input, respectively.

By comparing the length from the linear MMI, equation 2.18, with the equation above, a relation of ratio can be accomplish

$$\chi^T = \frac{W_0^2}{W_1W_0} = \frac{W_0}{W_1} [4] \quad (3.8)$$

As observed in figure 3.3 the MMI coupler MM waveguide is divided into a linearly down-tapered followed by a linearly up-tapered section. In order to the self-imaging properties

remain unchanged, the length of the MMI always needs to be adjusted according to the shape of the tapered section.

The width increase or decrease size will lead to a variation of distance between O_0 and I_1 and consequently it will create a phase difference between both MMI sections. The phase can be accurately controlled by the width variation of dW .

To acquire the required phase shifts between the tapered sections, the geometrical configuration needs to be fully adapted.

In comparison with the linear MMI, this tapered butterfly can reduce the size by the ratio of χ^T , same as a linear tapered. In terms of reduction both are equal, but the butterfly has the advantage of being possible to decrease the width in the middle of the MM. In the linear tapered MMI it is not possible to reduce the width if the gap size and waveguides widths are on the limit.

3.3.2 Parabolic Butterfly Multimode Interferometer

Other Butterfly MMI coupler have already been reported by David Levy et al.[5, 17] as a improvement for $N \times N$ MMI. This architecture is another example of a tapered applied in the middle position of the MM section. In figure 3.4, it is possible to observe where in the MM region, the tapered is applied.

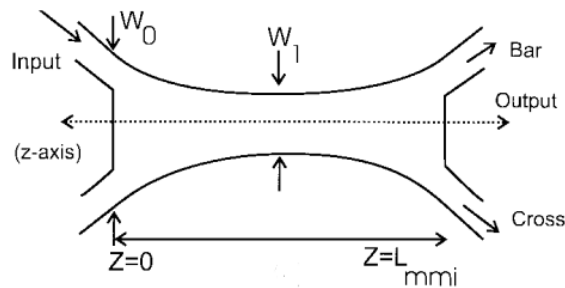


Figure 3.4: David Levy Parabolic Tapered MMI [5]

The width has decrease in the middle of the MM waveguide according to the parabolic function

$$W_M(z) = W_1 + (W_0 - W_1)(L_{MMI}/2 - z)^2(L_{MMI}/2)^2[5] \quad (3.9)$$

with z being the direction of the propagation.

As observed, the inputs are tilted, because it improves both power and splitting ratio and it can be obtained from

$$\theta = \tan^{-1}(4y \, d\Omega/L_{MMI})[17] \quad (3.10)$$

where y is the transverse waveguide position from the centre and $d\Omega = 1 - W_1/W_0$ is the normalized width variation. The fact that $dW_{MMI}/dz = 0$ is at $L_{MMI}/2$, minimizes the discontinuous phase changes utilized by Besse [4] [17].

$$L_\pi^T = \frac{4n_r W_0^2}{3\lambda_0} \frac{1}{\chi^T}[17] \quad (3.11)$$

The imaging length in the tapered MMI coupler is shorter than the linear straight by a factor of χ^T , as shown in equation 3.11. The factor χ^T is given by

$$\chi^T \equiv \frac{1}{2(1 - d\Omega)^2(1 + \gamma^2)} + \frac{\tan^{-1}(\gamma)}{2\gamma(1 - d\Omega)^2}[17] \quad (3.12)$$

with $\gamma = W_0/W_1 - 1$.

By comparing the normal length L_π from a W_0 width straight MMI with the length reduction obtained by equation 3.11 a relation can be attained, as shown below.

$$\frac{L_\pi^T}{L_\pi} = \frac{1}{\chi^T} [17] \quad (3.13)$$

This reduction, if working with a steady and equal power for both cases, is an higher quality architecture since, by comparing equations 3.3, 3.8 and 3.12, it allow us to reduce the length of the MMI slightly more than the other architectures. It can also be verify that the device length can be reduced regardless of number of ports, N . Although, as previously mentioned, the number of ports may force to increase the width size.

Chapter 4

Haar Transformation

Imaging compression explores a way of reducing the amount of information bits used in storing and transmitting. Nowadays Wavelet Transforms (WT) are being used as a method of imaging processing and compression [18]. Among the all the varieties of WT, the HWT [19] offers uncomplicated design and also fast computation can be easily implemented by optical planar interferometry [6]. The next chapter addresses an approach on HWT and, also, an already designed asymmetric coupler where the transform is applied.

4.1 Introduction

The computer and video-media have been evolving at a rapid pace, so the methods of imaging compressing must keep up this growth. This methods requires high performance, speedy digital video and audio capabilities. Images contain a large amount of hidden data, which is highly correlated. In a digital viewpoint an image can be seen as a group of pixels, where every neighbour pixels contain redundant information relative to each other [20]. Nowadays, the image processing and continuous or discrete transforms analysis are the typical processing techniques. In the signals compression, digital filtration and systems identification the commonly used transforms are based on sinusoidal basic functions [18]. The HWT is a DWT, which is a based sinusoidal function transform. It is an orthogonal function, in which the forward and inverse transforms requires only additions and subtractions. It is a simple, easy and efficient way to implement on the computer.

A wavelet is a wave that briefly oscillates, starting with a zero amplitude that increases, and then decreases back to zero. It produce a natural multi-resolution of every image, scaling image, including all the important edges, details images. Wavelets transforms, as observed in figure 4.1, have the ability to capture both low pass and high pass behaviours of an image, unlike the Fourier transform [6].

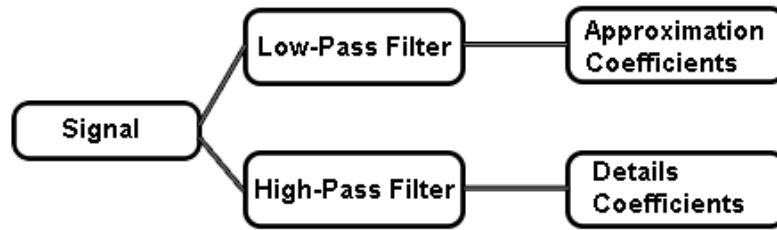


Figure 4.1: Process of a signal decomposition using multi-resolution analysis

The HWT entirely fits for image processing and pattern recognition as a result of its low computing requirements and performance, easy implementation by optical planar interferometry and efficient method of compression [20].

In short, HWT is a real and orthogonal transform which make it very fast. The orthogonality is relative to the signal splitting into a low and high frequency part and filters to deny duplicating information. Also the basis vector are sequentially ordered, it has a linear linear phase and also a perfect reconstruction. This proprieties result in a very good performance and speed in terms of computing time, in its simplicity, in a efficient compression method and in memory efficiency.

4.2 Theoretical implementation of the Haar Wavelet Transform

The ability to capture the low and high pass behaviour of an image has proved been very useful in image compressing, where the computational efficiency is the most crucial factor. The DWT can be implemented as a fast algorithm through computer coding scheme and can

also represent an image as a sum of wavelet functions, by using the signal into a set of detail and approximate coefficients. It starts with the lowest scale corresponding to the given image and computes the transform coefficients by iterating the filtering and sub sampling process.

The HWT, also known as Daubechies D2 Wavelet, is an example of multi-resolution analysis. The purpose of this thesis is to apply to Two-Dimensional (2D) signals, like images, wavelets decompositions that compress the image data. Using an averaging and differencing method one will be able to construct it.

The matrix 4.1 is the HWT matrix and it allow us to obtain, as output, an averaged and difference of the input signal.

$$S = \begin{bmatrix} \frac{1}{\sqrt{2}} & \frac{1}{\sqrt{2}} \\ \frac{1}{\sqrt{2}} & -\frac{1}{\sqrt{2}} \end{bmatrix} \quad (4.1)$$

In figure 4.2, the decomposition applied to an image and the sub-images results can be verified. This images results have a lower resolution and it correspond to a different band of frequencies.

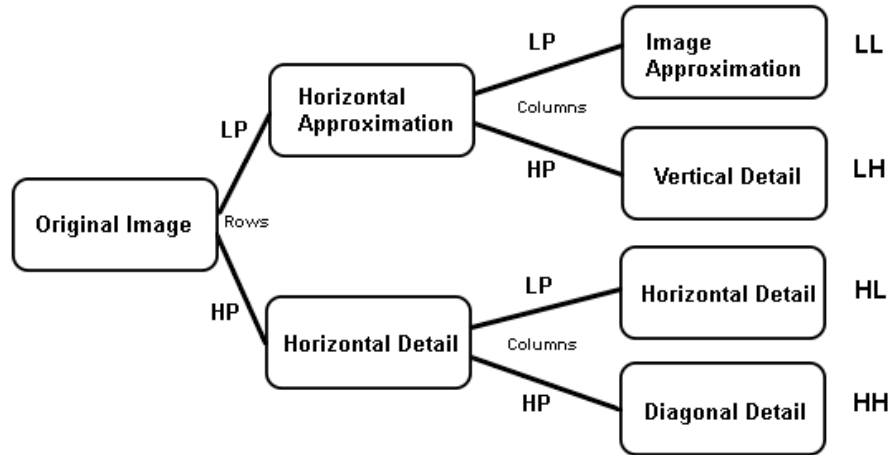


Figure 4.2: Band decomposition using wavelet transform

To obtain this it is necessary to have two different filters, a Low-Pass (LP) filter and an High-Pass (HP) filter. The LP is used to do an approximation and the HP to get the details of the image. This means that the filtering operation corresponds to the calculation of the average between two neighbours' pixels values and the difference between them, respectively.

$$\textbf{Low-Pass filter : } L(n) = \frac{n_i + n_{i+1}}{2} \quad (4.2)$$

$$\textbf{High-Pass filter : } H(n) = \frac{n_i - n_{i+1}}{2} \quad (4.3)$$

With an $N \times N$ input data matrix, it is necessary to apply the operation twice, horizontally then vertically. For each transform level, it is necessary to do it twice so that intensity variations all over the image are evaluated along the 2D. Applying both low pass and high pass filters on the rows obtaining two different matrices, L and H containing the horizontal approximation and the horizontal detail respectively. Next, on these subsequent matrices it is applied once again both LP and HP filters to its columns, and four different matrices are obtained: LL, LH, HL and HH. The LL corresponds to the average of the original matrix while the other matrices are the vertical, horizontal and diagonal details, respectively. By repeating this decomposition process it is possible to obtain higher-level transforms [21]. It is possible to reconstruct the original image without losses if no quantization is applied, which means that a lossless image compression can be achieved with HWT.

4.3 Haar transform - image processing and compression

The image processing and compression based on the Haar transform can be divided in four main stages, the first includes light detection, after there is a block for applying the Haar Optical Wavelet Transform, follow by a compression block and for last the data encoding section [6].

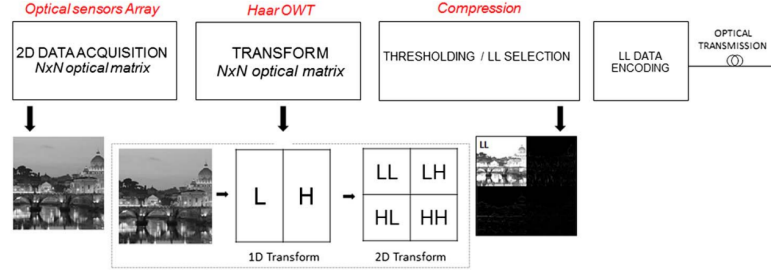


Figure 4.3: System building blocks for Haar optical wavelet transform based on image processing and compression [6]

As observed in figure 4.3 the first stage is the acquisition one. The $N \times N$ input matrix is obtained by optical sensors that capture light and also are responsible to obtain 2D data sampling. After, the matrix is ready to pass through the HWT block. Here is where the the image proprieties are extracted by being decomposed by the LP and HP filters.

The matrix 4.4 equation represents the $N \times N$ input data matrix sampled at the acquisition stage, the HWT scattering matrix for a One-Dimensional (1D), a_i coefficients, and the resulting scaling c_{ij} and detail d_{ij} coefficients, with i and j as transform level and index, respectively, obtained from the filters. Due to 2D input matrix, it is necessary to apply twice this process, for each transform level, in both vertical and horizontal components.

$$\begin{bmatrix} \vdots \\ c_{10} \\ d_{10} \\ c_{11} \\ d_{11} \\ c_{12} \\ d_{12} \\ \vdots \end{bmatrix} = \frac{1}{\sqrt{2}} \begin{bmatrix} 1 & 1 & 0 & & 0 & 0 & 0 \\ 1 & -1 & 0 & \dots & 0 & 0 & 0 \\ 0 & 0 & 1 & & 1 & 0 & 0 \\ & \vdots & & & \vdots & & \\ 0 & 0 & 1 & & -1 & 0 & 0 \\ 0 & 0 & 0 & \dots & 0 & 1 & 1 \\ 0 & 0 & 0 & & 0 & 1 & -1 \end{bmatrix} \begin{bmatrix} \vdots \\ a_0 \\ a_1 \\ a_2 \\ a_3 \\ a_4 \\ a_5 \\ \vdots \end{bmatrix} \quad [6] \quad (4.4)$$

Afterwards, the compression block is responsible for the extraction of the higher-frequency

components by applying the filtering operation at the LL sub-band. The other sub-band are ready to be stored,transmitted or discard. After compression and encoding, the data stream is forwarded through the optical channel.

To recover the transmitted data at the endpoint, an inverse system is provided to decode and dequantize the information. It is also necessary to apply the inverse HWT using its matrix and the coefficients.

4.4 Optical Haar Transform Network Implementation

To be possible to apply this system to compress 2D data images it is require to have a single Three-Dimensional (3D) module. This module is based on a Magic-T network, due to its proprieties of average and difference between each optical input. This 3D network allows,through the scattering matrix, equation 4.4, to implement and obtain at the same time LP and HP filtering on 1D [6].

Using a 2×2 matrix, with coefficients a_0, a_1, a_2 and a_3 from the matrix in 4.4, the first result produced by the HP and LP filtering are the detail and scaling coefficients from the horizontal dimension. This process needs to be repeated after the operation to also obtain the vertical coefficients. Afterwards, the scaling c_{ij} and detail d_{ij} coefficients are obtained, where i is the filtering step on each dimension and j is the coefficients index, corresponding to the first level of HWT.

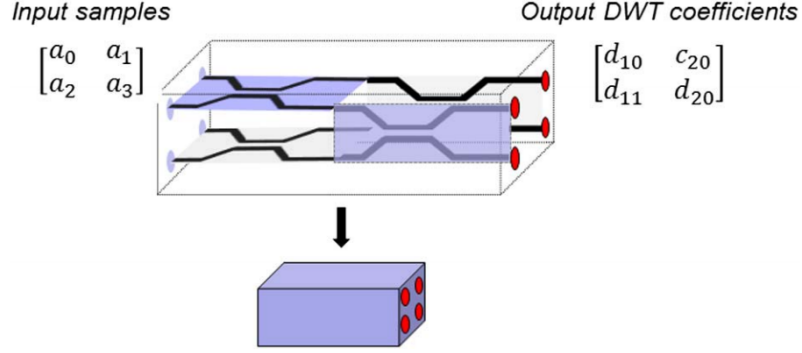


Figure 4.4: 3D basic module for the first level optical 2D Haar Transform [6]

This structure can be scaled by doing a basic model cascade from figure 4.4, then a $N \times N$ 3D scheme for the optical DWT can be achieved, allowing us to obtain the successive levels of HWT.

This module scheme, however, was considered for lossy compression techniques, which means that some data is going to be discarded in order to gain more compression delivering less information to the inverse transform. Nevertheless, the lossy compression techniques are easier to implement, rather than lossless, and are capable of achieving much higher compression rates at the cost of a small amount of reconstruction error [22]. Given the human visual sensitivity for low-frequencies components, by providing more relevance to these sub-bands making them more precise one can have a close lossless compression at human eyes.

4.5 3-dB Asymmetric Haar Coupler Design

An optical approach was already reported [6, 7] based on 3-dB asymmetric couplers. This kind of couplers, also known as Magic-T, due to the average and difference outputs can reproduce the Haar matrix used in the filtering process.

To perform the first order HWT it is used an asymmetric coupler based on coupled mode theory Coupled Mode Theory (CMT). This method states that when optical power is launched at a waveguide from an array of coupled waveguides, the power is exchanged

between the guided modes from each waveguide of the array [23].

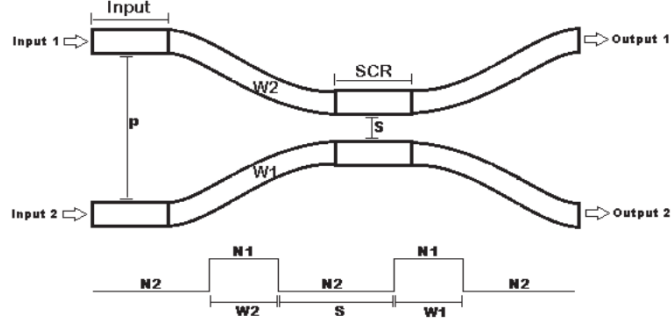


Figure 4.5: Schematic of the 3-dB asymmetric coupler [7]

This basic element is an optical asymmetric coupler whose scattering matrix exactly reproduces the required operations, the average and the difference between each optical input pair, as shown in matrix equation 4.1. After designing the coupler, the output values of power and phase from table 4.1 were obtained through simulations.

Table 4.1: Output values from the simulated 3-dB asymmetric coupler [7]

Input		Wider Waveguide	Narrowed Waveguide
Output			
Narrowed Waveguide	Power (W)	0.5	0.5
Narrowed Waveguide	Phase ($^{\circ}$)	1.03	-176.91
Wider Waveguide	Power (W)	0.5	0.5
Wider Waveguide	Phase ($^{\circ}$)	-0.48	1.60

The $\pi@3 - dB$ condition, which means two non identical waveguides designed with the requirements to have a maximum coupling of 50% and the output waves have to be in phase (sum) with the input for wider waveguide and have 180° (π) phase difference (subtraction) for the narrower waveguide input [6], is required for the Haar matrix image processing. As observed in the table 4.1 this condition was obtained. The coupler has approximately π phase difference between both waveguides and the same input power on the outputs.

The image rating parameters obtained acquaint the capability of the Haar approach and the ability to perform optical and passive compression. Although it had a good performance, this system can be improved.

One solution is using an MMI since it is possible to achieve the $\pi@3 - dB$ condition with it [9]. It has low power imbalance, compactness, low cross-talk and the better extinction ratio when compared to couplers. MMI have also an ease of fabrication and are less sensitive to fabrication tolerances. The most important characteristic is the reduce size when comparing it with the coupler.

Chapter 5

Magic-T exploratory analysis

HWT have already been implemented on integrated optics, as reported before. The Magic-T proprieties are the most relevant factor for this implementation. Some studies with $N \times N$ and $N \times M$ MMI, asymmetrical couplers and with Y-junctions were already reported. The next sections will evaluate the implemented MMI devices and techniques used to achieve the Haar matrix.

5.1 8 x 8 Multimode Interferometer Coupler Magic-T

For the same project in which this thesis is inserted, a possible solution was already revealed by Guilherme Cabral [9]. By using Soldano et al. equations 2.28 and 2.29, a phase relation was establish for $N \times M$ MMI, where $N \geq 1$ and $M \geq 1$.

As it was reported, when applying the symmetric and paired interference mechanism it was impossible to find 180° phase differences between outputs, which makes impossible to achieve the Magic-T characteristics of sum and difference. The only possible solution was found using general interference mechanism. By doing an investigation about the different varieties of MMI couplers, Guilherme Cabral found that there was a specific case that matches with proprieties needed for the Haar approach. In the table 5.1 it is possible to recognize it.

Table 5.1: Phase difference between the 8 x 8 MMI ports [9]

	Output 1	Output 2	Output 3	Output 4	Output 5	Output 6	Output 7	Output 8
Input 1	180.0°	157.5°	337.5°	270.0°	450.0°	337.5°	517.5°	360.0°
Input 2	157.5°	180.0°	270.0°	337.5°	337.5°	450.0°	360.0°	517.5°
Input 3	-22.5°	270.0°	180.0°	337.5°	337.5°	360.0°	450.0°	337.5°
Input 4	270.0°	-22.5°	337.5°	180.0°	360.0°	337.5°	337.5°	450.0°
Input 5	-270.0°	337.5°	-22.5°	360.0°	180.0°	337.5°	337.5°	270.0°
Input 6	337.5°	-270.0°	360.0°	-22.5°	337.5°	180.0°	270.0°	337.5°
Input 7	-562.5°	360.0°	-270.0°	337.5°	-22.5°	270.0°	180.0°	157.5°
Input 8	360.0°	-562.5°	337.5°	-270.0°	270.0°	-22.5°	157.5°	180.0°

By injecting signal at input 1 and 4, the Magic T properties can be obtained through output 3 and 7. As observed at output 3, the response for both input 1 and 4 is the signal sum. This can be observed since the phase is equal between them. At output 7 there is an 180° phase difference between ports, which means that port is a subtraction of input signals.

The disadvantage of this design is the power. With an 8 x 8 MMI the ratio of power on each output port is 1/8 of the input power due to the eight images that are created. This means that for an overlap, considering both outputs, it is possible to only take advantage of 1/4 of the power provided to the MM section.

Guilherme Cabral [9] used a Beam Propagation Method (BPM) simulation to get the power behaviour from the MMI. It is an approximation technique for slowly simulating light propagation in optical waveguides, which supplies a only forward propagation for larger optical components [24].

By using the superposition principle, it was possible to calculate the overlap output power. When having $1mW$ at each input, by this principle one would obtain $2mW$ of input power. The assumption is to obtain $2 \times 1/8$ of that power in each output guide, if the behaviour was an uniform splitter. Since the MMI creates the addition and difference in the two specific port, one output should have $0mW$ and the other output should have $4/8$ of the $2mW$ provided.

Table 5.2: 8 x 8 MMI coupler output power measures[9]

Power (mW)			
Input ports (port 1 and 4)		Output ports (port 3 and 7)	
1	1	0.497	0

As observed on table 5.2 the power obtained from the simulations tests is closed to the theoretical values, which proves that the operations of addition and difference are possible to implement with this device.

5.2 2 x 3 Multimode Interferometer Coupler Magic-T

Salwa El-Sabban et al [8] proposed and examined two different structures as a Magic-T solution, one based on a Y-junction and other on a MMI. This second structure was designed by using the self-imaging technique and it was verified by the use of BPM.

The main idea of the Magic-T is based on self-imaging and with this technique is possible to build a combiner that allows us to have the sum of the two inputs. To achieve it, Salwa El-Sabban et al. [8] reported that is necessary to use a separation of half of the effective width of the fundamental mode, $W_e/2$, and an even symmetry around $x = \pm W_e/4$ at the input ports. The length value is given by the linear MMI formulas presented in chapter 2,

$$L = p(3L_\pi)/8[8] \quad (5.1)$$

where $p = 1, 3, 5, \dots$ and $L_\pi \approx 4n_r W_e^2/3\lambda$.

The MMI has fixed values for width and length for each section, two input access waveguides and three output waveguides, as observed in figure 5.1.

signals and a direct image of two out-of-phase signals.

A BPM simulation was made by Salwa El-Sabban to verify if the design suits the characteristics of the Magic-T and if it is consistent with the theoretical values. The study was applied to the MMI on figure 5.1 with the same parameters values. The reason why the output access waveguides are S-shaped is to reducing the coupling between them in order to reduce the losses.

Using the defined length, the optical field distributions were calculated in the structure for in- and out-of-phase excitation.

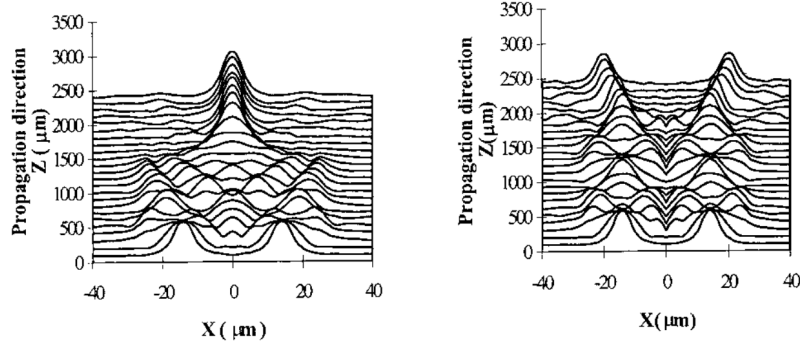


Figure 5.2: Optical distribution in the MMI structure for in-phase (left) and out-of-phase (right) excitation [8]

It is possible to notice from figure 5.2 that when the inputs are in-phase it is possible to obtain the addition on the central output waveguide and the difference on the other two. If the inputs have a 180° phase between them, out-of-phase, the central output waveguide is the one with the difference and the other two waveguides have the addition.

The frequency response of the structure is shown on figure 5.3. It is a relation between the input and output.

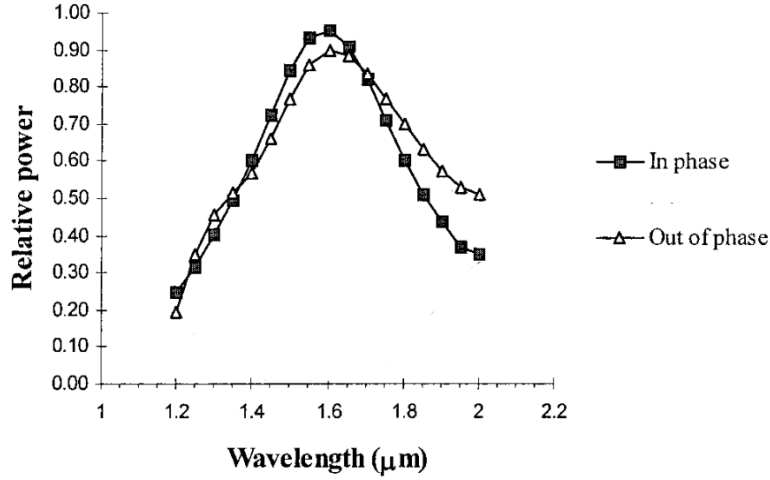


Figure 5.3: Redrawn graphic from the frequency response of the MMI device [8]

As observed in the figure 5.3, in a window from 1500 to 1700 nm, the relative power is always greater than 0.8, which means that the device, for this range, only has a 0.2 maximum relative power loss. At the wavelength of 1600nm, the relative power is close to 0.95 to in-phase and 0.90 to out-of-phase.

This design is better than the one presented before. Although it has a wider length, the power performance is superior.

5.3 Multimode Interferometer couplers with arbitrary power coupling ratios

A method for obtaining variable power splitting ratios using MMI couplers was presented by Thanh T. Le and Laurence W. Cahill [25]. The purpose of the paper was to present a method that could make the MMI having arbitrary power splitting ratios by etching the waveguides at a special location. The etching depth and its length adjusted the refractive index of that location, creating a phase shifter.

For a 3-dB 2 x 2 MMI based on restricted imaging mechanism, the length must be half of the beat length of the two lowest order modes, $L = L_{\pi}/2$. The MMI transfer matrix can

then be described as

$$M_{MMI} = \frac{1}{\sqrt{2}} \begin{bmatrix} 1 & j \\ j & 1 \end{bmatrix} [25] \quad (5.4)$$

Using this couplers, a connection between two equal ones was made. With a phase shift region in the middle of them, it was possible to obtain different powers. There are some methods to modulating the refractive index in order to achieve such phase shifter, but in this case the pattern was realized by etching.

Later Trung-Thanh Le [26] did a research similar to the work previously carried out, but it had more focus on HWT.

The MMI coupler is a effective element in optical signal processing, since the basic operations of sum and difference can be implemented by simply using some small modifications [26]. Over again, using equation 2.28 and 2.29, the phase differences between the 2 x 2 MMI can be verified.

Table 5.3: Phase difference between 2 x 2 MMI

	Output 1	Output 2
Input 1	180°	90°
Input 2	90°	180°

There are two distinct approaches to obtain a transfer matrix related to the HWT. The first is with restricted interference and the other with general interference MMI couplers, with lengths $L_{RI} = L_{\pi}/2$ and $L_{GI} = 3L_{\pi}/2$, respectively. The transfer matrices can be written as

$$M_{RI} = \frac{e^{j\phi_{RI}}}{\sqrt{2}} \begin{bmatrix} 1 & j \\ j & 1 \end{bmatrix} [26] \quad (5.5)$$

$$M_{GI} = \frac{e^{j\phi_{GI}}}{\sqrt{2}} \begin{bmatrix} 1 & -j \\ -j & 1 \end{bmatrix} [26] \quad (5.6)$$

where ϕ_{RI} and ϕ_{GI} are constant phase from restricted and general interference, and L_π is the beat length of the two lowest-order modes. By adding phase shifters at an input and output waveguides for both MMI_{RI} and MMI_{GI} , the overall transfer matrix has the form

$$M_\phi = \frac{e^{j\phi}}{\sqrt{2}} \begin{bmatrix} 1 & 1 \\ 1 & -1 \end{bmatrix} [26] \quad (5.7)$$

where the ϕ is equal to the phase of restricted or general interference. One can see that the above matrix 5.7 has the same general form as the first order HWT without the phase factor, $e^{j\phi}$.

A phase shifter of $\pi/2$ will allow to obtain the Magic-T proprieties in a 2 x 2 MMI, since it will add a $\pi/2$ phase in one input and output as observed in table 5.4

Table 5.4: Phase difference required for the Magic-T

	Output 1	Output 2
Input 2	180°	90°+ 90°
Input 1	90° +90°	90° +180°+ 90°

Therefore, the first order HWT can be obtained using this $\pi/2$ phase shift structure.

The extension of this study had a focus on theoretical topics that are not relevant for the Magic-T, so it was not possible to withdrawn power values to compare with the other architectures presented.

Chapter 6

Projecting novel architectures for Haar Wavelet Transform

With the objective of finding a solution for implementing the HWT with a MMI device, a wide study, based on the ideas presented in the preceding chapters, was performed. Based on the Salwa El-Sabban et al [8] a first idea emerged. This MMI had some limitations and had to suffer some changes. From this design another solution was found through simulation methods. This next chapter explains the procedures carried out to design the MMI in order obtain both solutions and the results retrieved from simulations on the software OptoDesigner PhoeniX SoftwareTM.

6.1 Foundry introduction

With the evolution and development of integration technology, the search needs of fabrication arise. In the photonics branch, number of photonic foundry owners have opened their fabrics to external users. These companies are entitled as foundries and they develop processes, in close cooperation with the customer, for the specific ordered components and requirements [27]. This approach has led to a reduction of the entry costs, since the users do not have to share the costs of their own cleanroom.

In the fabric process two major integration technologies were identified, Indium Phos-

phide (InP) and Silicon on Insulator (SOI). InP technology supports the highest degree of functionality. SOI offers most of the InP functionalities but with a better performance and lower cost due to its compatibility with complementary metal–oxide–semiconductor (CMOS) technology. Later another technology with dielectric waveguides was added, designated as TriPleX. All these platforms started by providing open access for research purpose. The Joint European Platform for Photonic Integration of Components and Circuits (JePPIX) platform appeared to the InP based integration technology of Communication technologies; Basic Research and Applications (COBRA) institute of TU Eindhoven. After the platform technology of Oclaro and Fraunhofer-Gesellschaft Heinrich-Hertz Institute (FhG-HHI) appeared. Next the ePIXfab platform to the SOI technology of IMEC and LETI and lastly the TriPleX platform to the technology of Lionix. With less expenditures in the PICs manufacturing, Process Design Kit (PDK) are available, creating benefits from lists of manufacturing Building Blocks (BB) and their design rules [27].

The FhG-HHI was the foundry used to the development of the MMI due to the clarity and good structure of the design manual.

In order to increase the flexibility for the implementation of PICs, FhG-HHI provides three different waveguides with height differences that can be used in the platform, the E200, E600 and E1700. The number from these waveguides corresponds to its height [28].

Analysing the design manual [28] it was possible to identify that the best waveguide to use is the E1700 since it has less propagation losses in waveguides with more than $2\mu m$.

The minimum gap size between adjacent waveguides must be $1.5\mu m$ and the minimum size for the waveguide width is $1.0\mu m$. For a monomode waveguide this width must be smaller than $2.7\mu m$.

The refractive index used is 3.258, with air as background with unitary index, 1. These values will suffer alterations due to some specifications from the manual, and they can be obtained through cross section simulation methods in special film mode method.

For the MMI designs the wavelength was $\lambda = 1.550\mu m$. During the simulations tests the C-band, $1.530 - 1.565\mu m$, was used to ensure a good MMI behaviour.

6.2 2 x 3 Multimode Interferometer Coupler

Analysing the El-Sabban [8] design, it can be seen that it is possible to reduce the MMI size by decreasing its width. The size decrease will reduce the number of propagated modes but it will manage to keep the sum and difference proprieties.

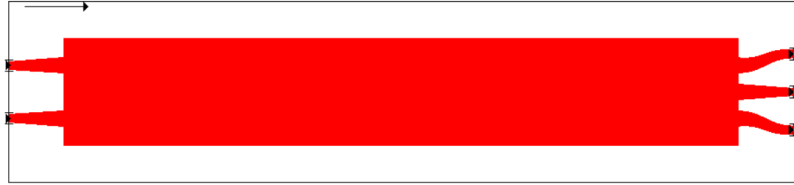


Figure 6.1: El-Sabban [8] 2 x 3 MMI design adaptation

In order to reduce the size of the MMI, a width value of $14\mu m$ was set. This would ensure the minimum gap size between waveguides. The inputs are placed at a position of $\pm W_e/4$ and one output is placed at a central position and the other two also at $\pm W_e/4$, where W_e is the MMI width. By using the equation of the beat length of the two lowest-order modes,

$$L_\pi \simeq \frac{4n_r W_{e0}^2}{3\lambda_0} \quad (6.1)$$

the value of the calculated length was $542.13\mu m$. The MMI length needed to achieve three images on the output and the magic-T characteristic is, according to equation 2.37,

$$L_{MMI} = \frac{3L_\pi}{2} \frac{3}{4} = 609.89\mu m \quad (6.2)$$

Both access waveguides have $1\mu m$ in the smallest taper zone and $2\mu m$ in the largest zone, which is the one making contact with the MM waveguide. Both have a length of $L_{tap} = 20\lambda\mu m$.

Running a BPM simulation with the parameters values above, the following output values were obtained

Table 6.1: Phase and Overlap relations for both inputs working separately

Output Waveguides	Bottom as Input			Upper as Input		
	Bottom Port	Middle Port	Upper Port	Bottom Port	Middle Port	Upper Port
Overlap Power (W)	0.223	0.443	0.204	0.204	0.443	0.223
Phase Difference (°)	152.09	-27.87	-27.64	-27.61	-27.85	152.03

Magic-T proprieties are verifiable by analysing the table 6.1. By injecting signal in the bottom input port, a phase of $\alpha \simeq -27^\circ$ in the middle and upper is reached and a phase of $-\alpha \simeq 152^\circ$ in the bottom output was obtained. When the signal is injected in the upper input port it has a phase $\beta \simeq -27^\circ$ in the middle and bottom and a phase $-\beta \simeq 152^\circ$ in the upper output. It can be concluded that the outputs have a sum and two differences.

Table 6.2: 2 x 3 MMI output signals

Bottom port	Middle Port	Upper Port
$\beta - \alpha$	$\alpha + \beta$	$\alpha - \beta$

Despite having a sum and two differences this solution is not good for applying it on an Haar network, figure 6.2.

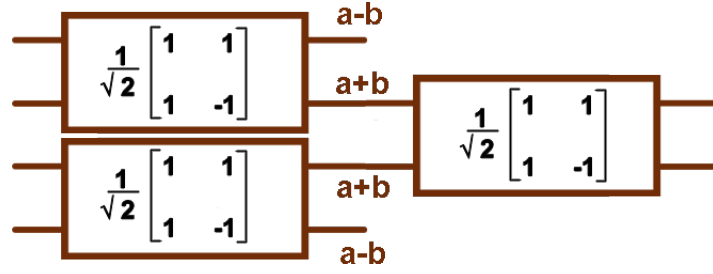


Figure 6.2: Haar Network schematic

Since there are two inputs and three outputs it would be necessary to implement another 2×1 MMI to add both difference output ports in order to obtain a 2×2 device. This would increase the device length and complexity. Even though there are other complications when using this idea. By adding our difference outputs, $\alpha - \beta$ and $\beta - \alpha$, the result would be null since $(\alpha - \beta) + (\beta - \alpha) = 0$. So it is necessary to find a solution that adds a 180° extra phase to one of the difference output waveguides, in order to get a signal inversion, $-(\alpha - \beta)$.

The relative phase changes along the length of the waveguide [29], so modifying one of the outputs is possible to obtain a 180° phase shift. By doing simulations on monomode waveguides, a solution was found. Through increasing the length of the bottom output by $9.4\lambda\mu m$, it is possible to achieve $\alpha - \beta$ on both edge output waveguides and $\alpha + \beta$ in the middle one.



Figure 6.3: 2×3 MMI with a phase shifter

With the waveguide increased length, the following values were achieved by running the BPM simulation.

Table 6.3: Phase and Overlap relations for both inputs working separately

	Bottom Input			Upper Input		
Output Waveguides	Bottom Port	Middle Port	Upper Port	Bottom Port	Middle Port	Upper Port
Overlap Power (W)	0.204	0.444	0.224	0.223	0.443	0.199
Phase Difference (°)	-27.59	-23.42	-27.85	152.06	-27.76	157.02

Altogether, doing the simulation with both inputs signal, as observed in table 6.4, an overall power of ≈ 1.776 W was obtained. Using the Insertion Loss (IL) equation, where P_i is the input power and P_o is the output power,

$$I_L = 10\log_{10}(P_i - P_o) \quad (6.3)$$

this power is equal to -6.498 dB.

Table 6.4: 2 x 3 MMI output power signal as input sums

Bottom Port Power (W)	Middle Port Power (W)	Upper Port Power (W)
0.0004	1.7759	0.0007

Although this solution has already the correct phase relations, it continues to have three outputs. As said, it is required to add a second MMI to sum both difference outputs.

The presented solution is superior than Guilherme Cabral's idea [9]. Although it has an increase in length, due to the incorporation of the second MMI, it has a better power performance, which makes it superior.

By applying a change, similar to this one presented, on a 2 x 2 MMI access waveguides, it would be possible to make an higher quality solution. The solution would have the two required outputs instead of the three here obtained.

The next section will explain the approach used to reach the Magic-T with a linear MMI.

6.3 2 x 2 Linear Multimode Interferometer

The next solution emerged from an adaptation of the design presented before and Trung-Thanh Le [26] MMI with arbitrary power coupling ratios.

Setting the width value of the MM section as $8\mu m$ and using again the equation of the beat length of the two lowest-order modes 6.1 it is possible to obtain a length of $L_\pi = 177.02\mu m$. Placing the access waveguides at $\pm W_e/4$ while having a length of $3L_\pi/2$, two-fold images with a power ratio of 0.5 for each port are achieved. As Guilherme Cabral [9] and Thanh T. Le et al. [25] reported, it is possible to obtain the 180° and 0° phase difference out of a linear MMI, table 5.4. This can be verified if a difference of 90° between ports can be obtained, by using phase shifters before one input and one output. As observed in table 6.5 by adding the phase shifters to the phase of a linear 2 x 2 MMI it is possible to get the sum and difference proprieties.

Table 6.5: Phase difference required for the Magic-T

	Output 1	Output 2
Input 2	180°	180°
Input 1	180°	360°

Through simulation methods and while studying comparisons between linear and tapered waveguides, one conclusion relative to monomode waveguides was drawn.

As the width changes along the access waveguide, also the effective refractive index suffers alterations from the light signal perspective. When the signal is transmitted through a not linear waveguide, although the refractive index is analytically the same, it creates alterations to the light propagation speed.

$$v_w = \frac{c}{n_r} \tag{6.4}$$

The signal propagation inside a rectangular waveguide with L_w length and W_1 width is different than inside a tapered waveguide with L_w length and W_1 and W_2 width, where $W_2 > W_1$. So it is possible to settle different light signals and consequently phase differences at the extremity of the access waveguides.

With this knowledge, a solution was achieved through simulations methods. Figure 6.4 presents a waveguide that works as a 90° phase shifter. The first block is a straight waveguide and the second is a tapered waveguide.

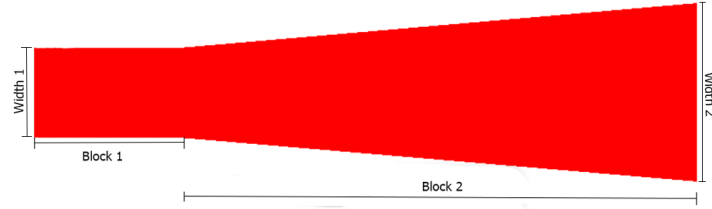


Figure 6.4: Phase shifter waveguide design

The parameters from the waveguide are presented in table 6.6, where the length values were estimated through simulations tests.

Table 6.6: Waveguide parameters value

	Straight	Tapered
Width 1 (μm)	1.000	1.000
Width 2 (μm)	1.000	2.000
Length (μm)	5.599λ	20.000λ

During the simulation to optimize this access waveguide it was realized that there is a periodicity of $3N \times 5.599\lambda$, where $N = 0, 1, 2, 3, \dots$, that adds a 180° extra phase to the phase shifter. Although for $N = 1$ there is a slightly improvement in terms of power, as observed in Appendix A, the phase variations are superior when in comparison with $N = 0$. When $N > 2$ the losses start to get over 20% so it starts to be worst than the required for the project. This waveguide needs to be added to one input and output of the MMI to create the phase shifter

of 90° , vital to the Magic-T, as shown on table 5.4.

The next figure is a schematic of the linear MMI with the waveguides already implemented on bottom access waveguides. As mentioned before, this MMI has $8\mu m$ width and using the equation of the beat length of the two lowest-order modes, equation 6.1, the value of $L_\pi = 177.02\mu m$ was achieved and consequently a value of $L_{MMI} = 3L_\pi/2 = 265.53\mu m$ to get the two-fold images.

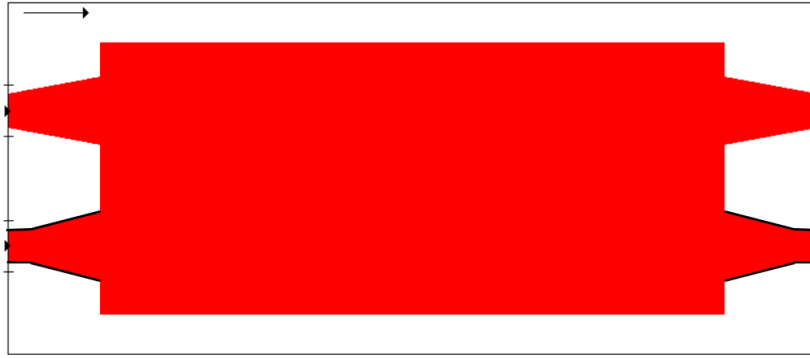


Figure 6.5: Linear MMI Schematic

It can be noticed from the figure above that the both upper access ports are normal tapered with waveguides and the bottom ports are phase shifter ports. The tapered waveguides were selected instead of straight waveguides, since it is possible to achieve more performance in the MMI with them. These waveguides have $W_1 = 1\mu m$ and $W_2 = 2\mu m$ width and the length is $L = 25.599\lambda$. The length is equal to the sum of the two blocks length from the phase shifter waveguide.

After designing the MMI with all the parameters on the software PhoeniX OptoDesignerTM a new BPM simulation was made. Using $1W$ of power as the reference value, the behaviour of the MMI and the output values of power and phase were withdrawn.

The next figure shows the propagation along the MM section, using separated input signals.

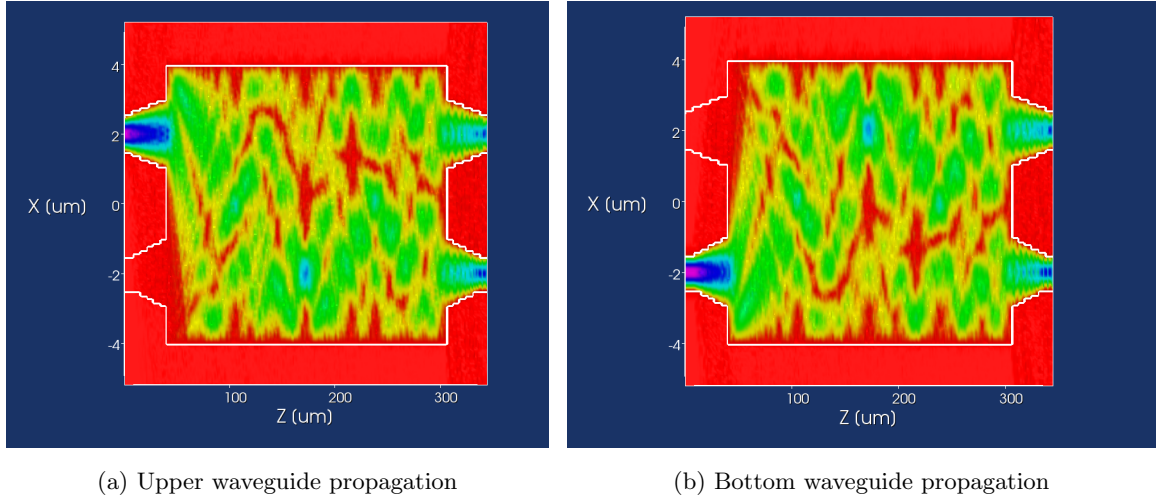


Figure 6.6: Power propagation along the 2 x 2 MMI with separated input signals

The output values obtained in the simulation above, for separated input responses, are presented in the table 6.7.

Table 6.7: Output power and phase

(a)	Upper Port	Bottom Port
Power (W)	0.473	0.485
Phase (°)	159.21	-20.93

(b)	Upper Port	Bottom Port
Power (W)	0.486	0.472
Phase (°)	-21.02	-21.08

It is possible to observe that bottom output (b) has no phase difference, while upper output (a) has 180° phase difference.

With both inputs, the simulation results are shown in the figure below.

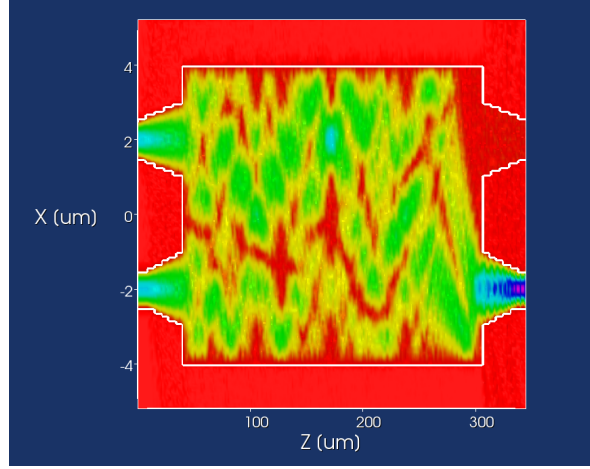


Figure 6.7: Power propagation along the 2 x 2 MMI

It is possible to conclude from figure 6.7 that the bottom port has the signal sum while the upper output has the signal difference. The power obtained from the simulation was 1.9112 W and 0.0009 W for the sum and difference, respectively.

Noticing that it is possible to achieve the Magic-T with the linear MMI it is necessary to acknowledge its performance within the C-band. Sweeping the BPM simulation through wavelengths between $1530\mu m$ and $1565\mu m$ it was possible to confirm that it has a good behaviour in this range. As observed in figure 6.8a and 6.8b, the overlap of output ports has an IL maximum of -8.801 dB when injecting the signal at the bottom input and -8.647 dB when using the upper input. The minimum is -14.172 dB and -14.558 dB, for bottom input and upper input, respectively.

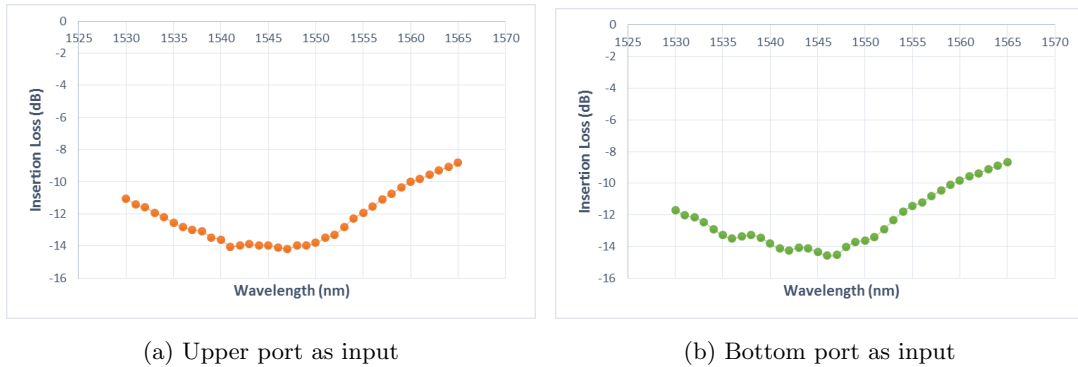
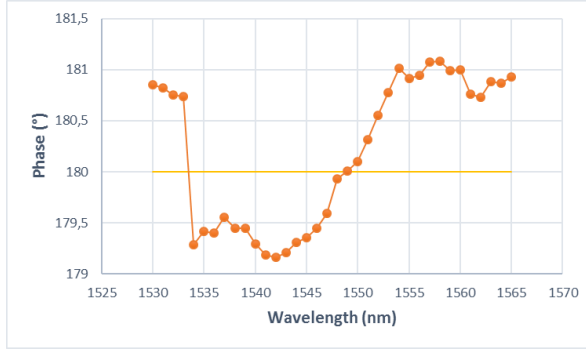
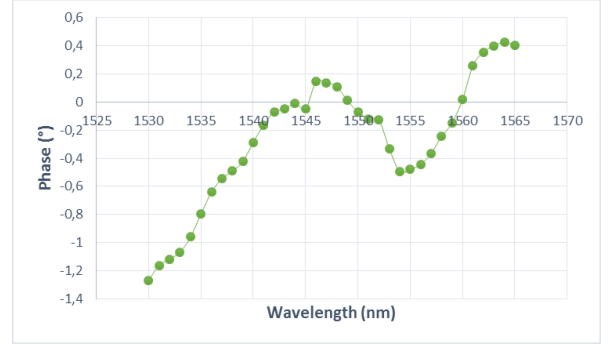


Figure 6.8: Linear MMI Insertion Loss

When referring the phase values, also through the C-band range, the maximum oscillating phase difference is 1.85° for difference port as input and 0.70° for the sum, concluding that also has a good phase response. In the figure 6.9a and 6.9b one can observe the sweep through the C-band and the phase difference for both outputs.



(a) Upper port as input



(b) Bottom port as input

Figure 6.9: Linear MMI phase performance

As an overall, with both input ports working, one can verify in figure 6.10 that the maximum IL is -5.605 dB at $\lambda = 1565$ nm and the minimum is -11.418 dB at $\lambda = 1547$ nm.

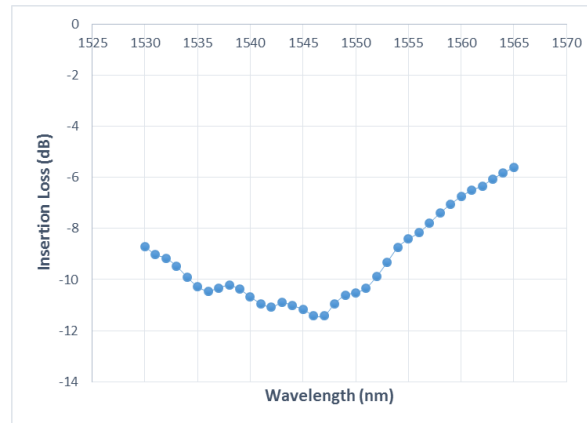


Figure 6.10: Overall Linear MMI Insertion Loss

As a conclusion it can be declare that the 2×2 MMI has minimum losses for the designed wavelength, it has good response for the C-band range and it has minimum phase variations for the same range.

As studied on chapter 3, it is possible to reduce the size of the MMI, without changing the border width, by applying a tapered zone on the centre of the MM section. The next sections will approach two different designs and which one is a better solution for the Magic-T.

6.4 2 x 2 Tapered Butterfly Multimode Interferometer

Since our MMI already has approximately the minimum width to be within the rules of the foundry, it is not possible to reduce the size with a linear tapered presented in section 3.2. With this, it is necessary to use a butterfly shape, by reducing the size in the middle of the MM waveguide.

Using the concept presented on chapter 3 an adaptation of the MMI was made and shaped to a tapered butterfly, figure 6.11. The waveguides did not suffer any change to the parameters values, neither the wavelength or the refractive index. The modification was applied to the MM section, by decreasing the width at the central position. At the length of $L_{MMI}/2$ the width was reduced to $6\mu m$. Using the equation 3.7 from Pierre A. Besse et al. [4], the MM length was determined. Using $W_0 = 8\mu m$ and $W_1 = 6\mu m$, the new length value is $L_{MMI} = 199.15\mu m$, reducing the length by $66.38\mu m$ comparatively to the linear MMI.

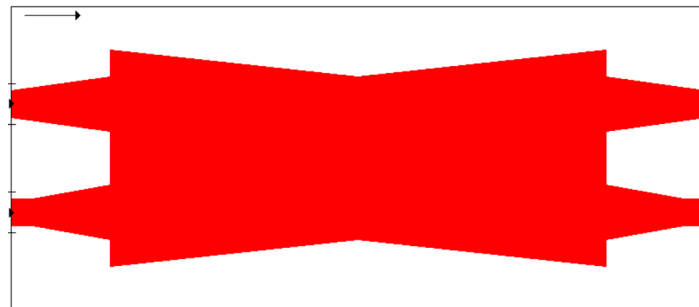


Figure 6.11: MMI Tapered Butterfly Schematic

Running the BPM with the new design it was possible to verify that the Magic-T properties remained almost unchanged, with only a slightly power decrease. As show on figure 6.12,

the bottom output waveguide is again the sum port and the upper waveguide is the difference.

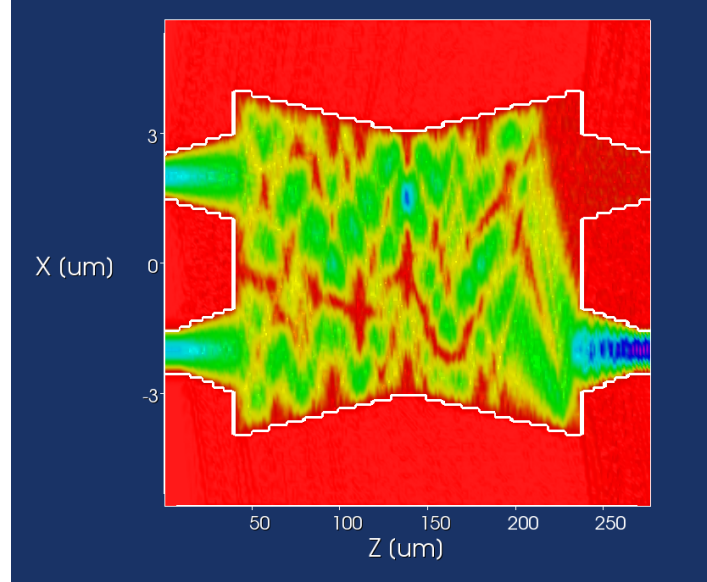


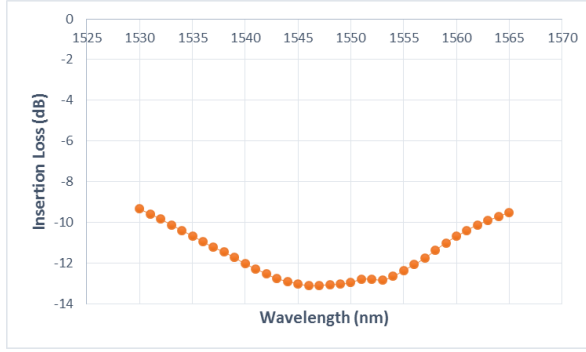
Figure 6.12: Power propagation along the 2 x 2 Tapered Butterfly MMI

Through the simulation one can retrieve the values of power and phase. Comparatively to the linear MMI values, it has a minor deviation of phase $\approx 0.2^\circ$ and a power decrease of $0.01W$. The output overlap results, obtained from separated inputs, are shown in table 6.8.

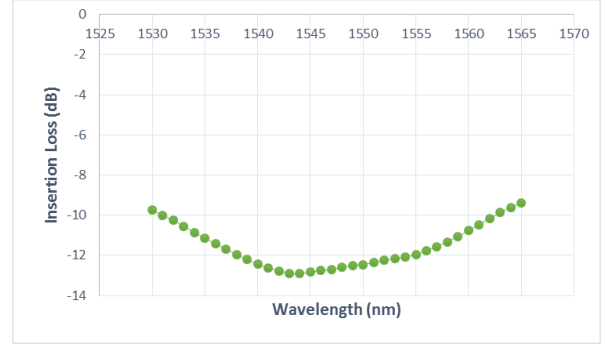
Table 6.8: Tapered Butterfly output phase and power

Inputs	Upper Waveguide	Bottom Waveguide
Overlap Power (W)	0.9495	0.9432
Phase Difference ($^\circ$)	180.2	-0.211

As simulated in the linear MMI, the performance in the C-band was measured with BPM simulation. The power behaviour is almost the same as in the linear one. By calculating the IL, it was possible to obtain the results of the output overlap, being -13.118 dB the minimum and -9.346 dB the maximum, when using only the upper input. For the bottom input signal the minimum obtained was -12.906 dB, while the maximum was -9.383 dB.



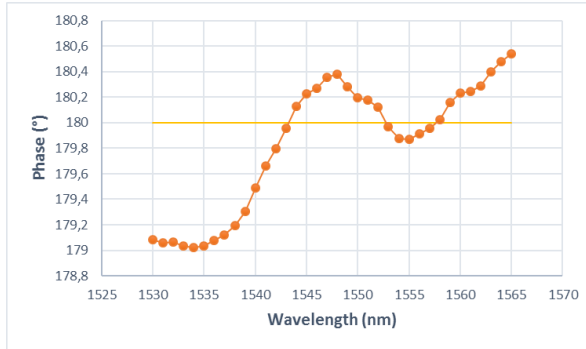
(a) Upper port as input



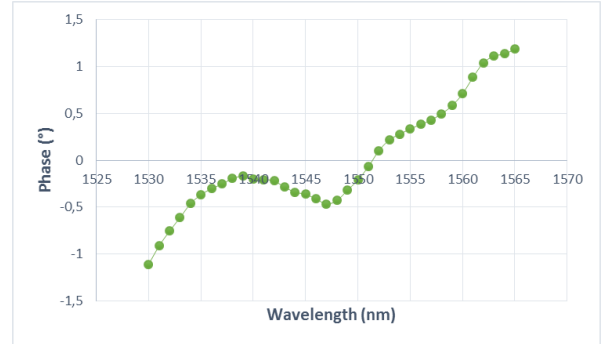
(b) Bottom port as input

Figure 6.13: Tapered Butterfly MMI Insertion Loss

Relatively to the phase, the maximum diversion is 0.92° for the upper port and 1.18° for the bottom one, as shown bellow.



(a) Upper port as input



(b) Bottom port as input

Figure 6.14: Tapered Butterfly MMI phase performance

Once more, using both inputs, the values of power were retrieved, through all the C-band range, figure 6.15. When comparing it with the linear MMI response, figure 6.10, it can be observed that the best power performance, although the design was made for $\lambda = 1550\text{nm}$, is at $\lambda = 1544\text{nm}$. It has more phase deviation from the required, but it has less IL with this wavelength.

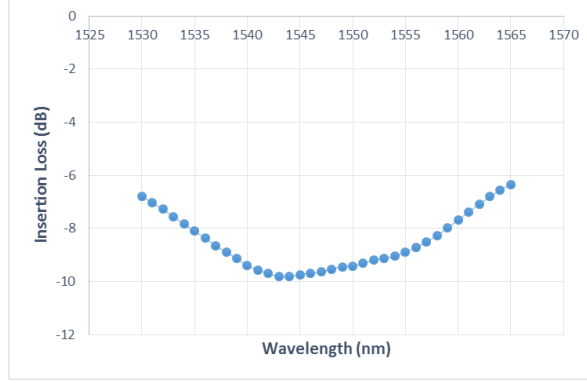


Figure 6.15: Overall Tapered Butterfly MMI Insertion Loss

This design has -9.813 dB of minimum IL at $\lambda = 1544nm$ and -6.340 dB at $\lambda = 1565nm$ as maximum IL.

6.5 2 x 2 Parabolic Butterfly Multimode Interferometer

The next design is based on David Levy et al. [5, 17] idea. It is a different tapered shape with the same possibility of reducing the length by decreasing the width at the central position of the MM section, without changing the proprieties of the linear MMI.

Over again without any change in the access waveguides, refractive indexes and wavelength just reducing the central width of the MM section to $6\mu m$. Using the software PhoeniX OptoDesignerTM basic functions, the MM section was designed as a parabola. Building it with two exponential functions, the first one decreasing and other increasing by a factor of 2, the parabolic MM zone shown in figure 6.16 was obtained. Through simulation methods the MMI was optimized to obtain the best length for it, resulting in a length of $L_{MMI} = 180.07\mu m$. This reduction is relative to the value $\chi \approx e/4$.

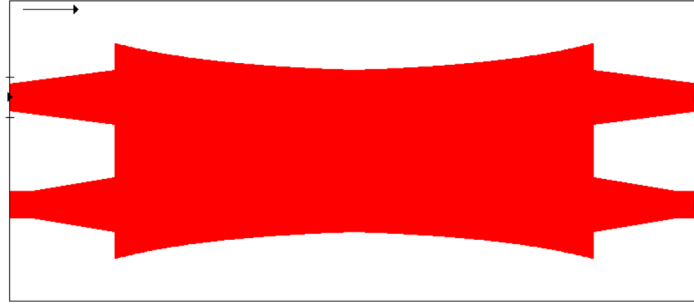


Figure 6.16: MMI Parabolic Butterfly Schematic

As done in the section above, by implementing the BPM simulation to the built design, it was possible to verified that the same proprieties were kept, where upper output waveguide is the difference port and bottom is the sum port.

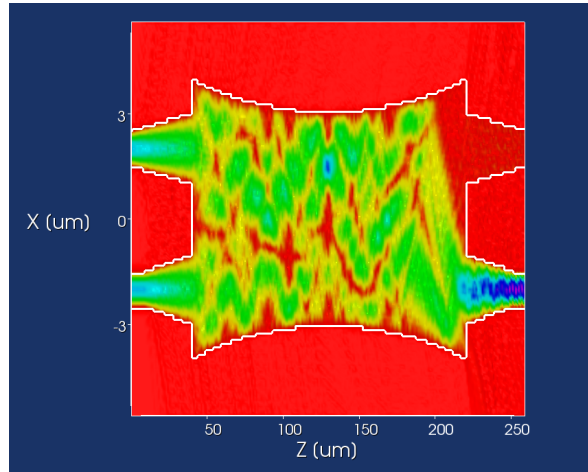


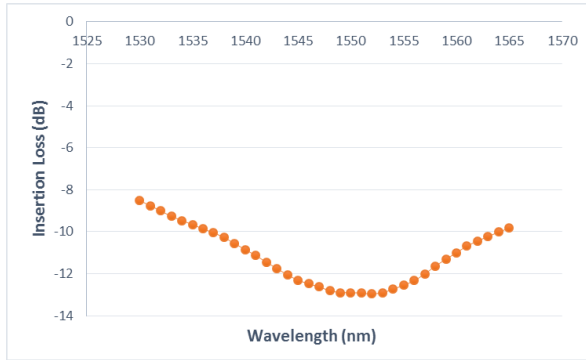
Figure 6.17: Power propagation along the 2 x 2 Parabolic Butterfly MMI

The values of power and phase collected from the simulation are approximately equal to the Tapered Butterfly MMI, where the phase suffers a deviation of $\approx 0.30^\circ$ and $\approx 0.21^\circ$, upper and bottom port respectively, and a power decrease of $\approx 0.012W$, as shown in table 6.9.

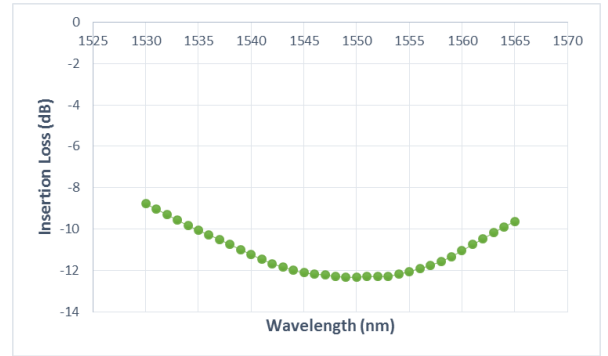
Table 6.9: Parabolic Butterfly output phase and power

Inputs	Upper Waveguide	Bottom Waveguide
Overlap Power (W)	0.949	0.941
Phase Difference ($^{\circ}$)	180.41	-0.28

Doing the sweep simulation on C-band range, it can be observed that the Parabolic Butterfly has the maximum power of 0.949 W at $\lambda = 1551nm$, and minimum of 0.859 W at $\lambda = 1530nm$ for the upper output waveguide. This means -12.923 dB and -8.515 dB of IL respectively. As for the bottom port, it has a maximum power of 0.942 W, at $\lambda = 1549nm$ and minimum of 0.868 W at $\lambda = 1530nm$, which means -12.327 dB and -8.782 dB of IL respectively. The overlap values of IL can be observed in the figure bellow.



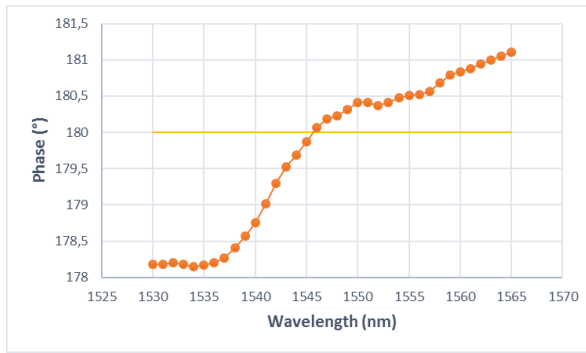
(a) Upper port as input



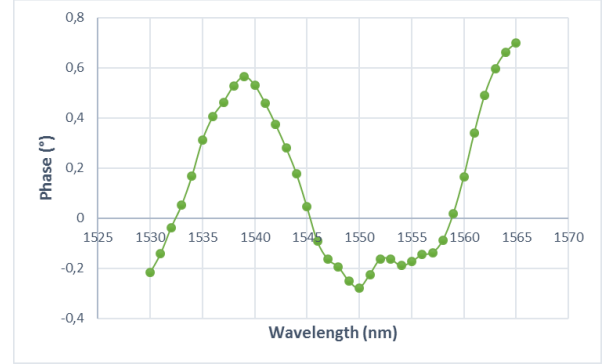
(b) Bottom port as input

Figure 6.18: Parabolic Butterfly MMI Insertion Loss

The phase, when comparing it with the standard values for the Magic-T, has a maximum diversion is 1.85° at $\lambda = 1534nm$ for the upper port and 0.70° at $\lambda = 1565nm$ for the bottom one, as observed in the figure below



(a) Upper port as input



(b) Bottom port as input

Figure 6.19: Parabolic Butterfly MMI phase performance

The maximum power performance is at $\lambda = 1549nm$ and the minimum at $\lambda = 1530nm$ as an overlap of both inputs. This corresponds to a maximum IL of -5.806 dB and minimum of $-9,320$ dB.

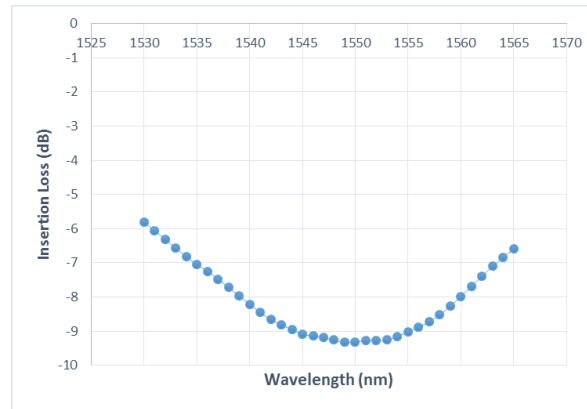


Figure 6.20: Overall Parabolic Butterfly MMI Insertion Loss

6.6 Final design optimization

After analysing all the designs developed, it was necessary to choose the one that suits as solution for the project. Doing a compilation of all the main parameters and values from the three MMI designs it was possible to define which was the best.

Table 6.10: Insertion loss of each MMI and main parameters

	Linear	Tapered	Parabolic
Insertion Loss (dB)	-11.418	-9.813	-9.320
Wavelength (nm)	1547	1544	1549
MMI Length (μm)	265.53	190.00	180.07

Interpreting the table values, the Parabolic Butterfly was the chosen, since it has the minimum length of all the three designs. When verifying the power loss there is a difference of 2.2% between the Parabolic and the Linear MMI, which is the best in terms of power.

From the theoretical information that was studied, it is possible to optimized the MMI by changing the position where to decrease the width in the MM section.

Firstly, it was necessary to adjust the place where the width is reduced to $6\mu m$. In order to find the best position to adjust the power, a BPM sweep was made, through a range of $[-5, 5]$, having as referential position the centre of the MM section $L_{MMI}/2$. From it was possible to conclude that by moving the minimum width position to $z = L_{mmi}/2 - 3\mu m$ a better power could be obtained, as observed in figure 6.21.

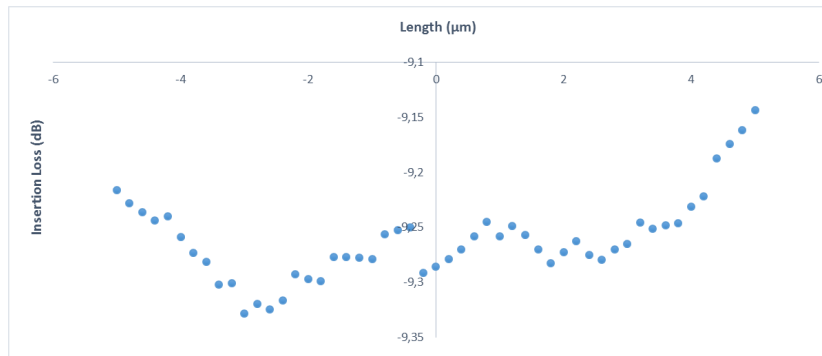


Figure 6.21: Position sweep for width reduction position

Defining the new position value and running the BPM simulation, new values of power were obtained for $\lambda = 1550nm$.

Table 6.11: Optimized MMI output phase and power

Inputs \ Outputs	Power (W)		Phase(°)	
	Upper Waveguide	Bottom Waveguide	Upper Waveguide	Bottom Waveguide
Upper Waveguide	0.4896	0.4582	167.81	-12.57
Bottom Waveguide	0.4597	0.4825	-12.56	-12.39
Both Waveguides	0.0005	1.8811	-12.48	179.20

As all the other simulations, having 1W as input power value in each access waveguide, the IL was calculated with the assistance of table 6.11, obtaining a value of -9.329 dB. Before optimizing the MM section the IL value was -9.320 dB, so when comparing with it, the improvement it was not that satisfactory.

To verify the full behaviour of the MMI another simulation was made in order to study its performance when the phase inputs had difference between each other. With a 180° phase difference between the input waveguides, it was possible to verify that, regardless of the input port where the phase is inverted, the outcome is the same. The output waveguide suffers an exchange between them, where the upper port is now the sum and the bottom is the difference. With this, it is possible to conclude that the proprieties are kept, as shown in figure 6.22.

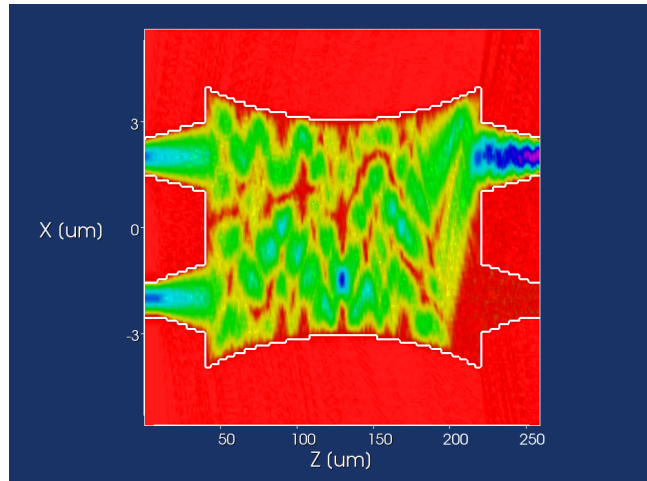


Figure 6.22: Magic-T performance with 180° extra input phase

Comparing this figure to figure 5.2, it is possible to establish a relation of equal behaviour between this MMI and the MMI presented by Salwa El-Sabban et al. [8].

6.7 Haar Network Implementation

After optimizing the MMI device, the Haar network must be applied. Designing it as a combination of three MMI, it was possible to verify the behaviour of the MMI when applied in a second order Haar network, as shown below in figure 6.23.

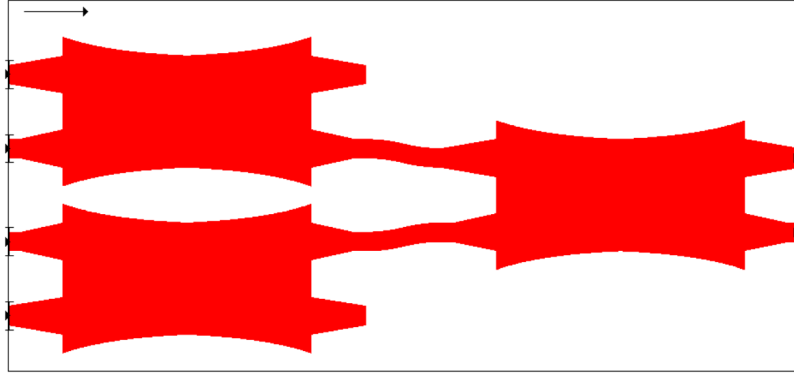


Figure 6.23: MMI Haar Network

To obtain the network first it is necessary to rotate symmetrically one MMI in order to have the sum outputs from each MMI in the middle. After, it was required to connect the first level of the network to the third MMI. The connection was made with a monomode waveguide in a S-shape, because it allows the reduction of power losses.

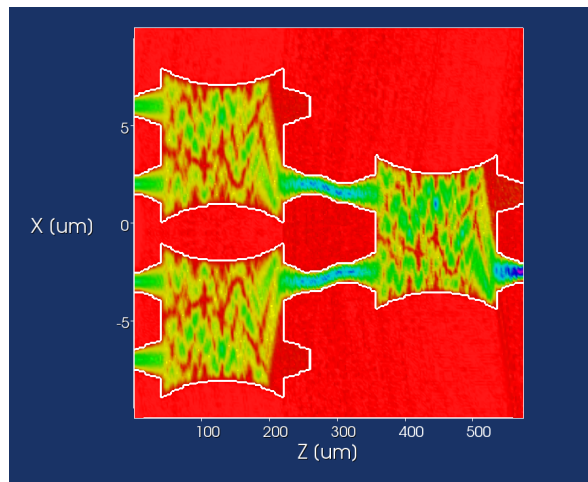


Figure 6.24: BPM simulation on the Haar Network

Running now the BPM simulation it was possible to verify the behaviour of sum and difference present in the Magic-Ts, figure 6.24. The first level, as said before, has a symmetry between the two MMI in term of output waveguides in order to provide an equal signal to the second level.

An overall study is presented in the table 6.12 bellow.

Table 6.12: Haar Network output phase and power

Inputs \ Outputs	Power (W)		Phase(°)	
	Upper Waveguide	Bottom Waveguide	Upper Waveguide	Bottom Waveguide
Upper MMI	0.9039	0.8538	60.85	-119.42
Bottom MMI	0.8615	0.8928	-119.07	-119.02
Both MMI	0.0005	3.4927	57.35	-119.22

As a last observation it is possible to conclude that the network has the same behaviour as a single Magic-T. The second level of the network uses the output sum ports from the first level and add them. With the power values from table 6.12 an IL value of -2.952 dB was obtained.

Chapter 7

Conclusion and Future work

This thesis had as main objective developing a possible optical tool that implements layers of optical compression, applicable to any type of signal. Since WT are being more used as a method of imaging processing and compression, this project was based on the HWT due to their uncomplicated design. Focusing on improving the already implemented architectures, the use of a MMI structure was the fundamental aspect to this implementation. To understand how to manage to develop the HWT on a MMI device, a work structure was done in order to guide and explain the solution made.

Two major theoretical concepts had to be learned and explained in order to develop the desired optical tool. Firstly the self-imaging principle, in which the MMI is based, is presented along all the equations of the different categories of MMI and possible architectures that can be adapted in this project. Then, to understand imaging processing and compression, an overview of the HWT was studied. Through a project already implemented, the theoretical approach was done as well as a small explanation of it. Finally, a brief introduction to the foundry used in our solution implementation with all the requirements and constant parameters values. With this large amount of information, some investigation was made in order to achieve a solution for the project.

After accomplishing a solution, having all the fundamental parameters known and calculated, using the OptoDesigner Phoenix SoftwareTM to design some solutions. Analysing the MMI behaviour and drawing some conclusions, a final solution was adopted and optimized.

The 2 x 2 MMI with access waveguides working as phase shifters was the best design. This device has -9.329 dB of IL and a length of $180.07\mu m$. When comparing this solution to the coupler [6, 7] which is implemented in the COMPRESS project, there is an improvement of more than 1/10 in size reduction. It has also a superior power performance relatively to Guilherme Cabral [9], since his solution only presented the use of half of the input power.

As future work there are two priorities when regarding the improvement of the Magic-T implementation with MMI. The first consists on improving the performance by the use of other foundry. Given the development of PICs, foundries are becoming even more complete in their BB list. By using other foundry in this architecture, it is possible to reduce the size and upgrade the performance of the solution. The other priority is based on the MMI definition. An MMI consists of a group of input single mode waveguides which define the input field of a wider MM section where the effects of interference of mode fields and single mode output waveguides [30] can be observed, which means that the interferences in a MMI must occur in the MM section. The solution presented uses the access waveguides to create interferences in order to achieve the phase required for the HWT. By changing the shape of the MM, as shown in appendix 2, it is possible to equal the phase properties of the Magic-T. This architecture must be explored due to the properties shown. By tilting the MM section with a calculated angle, the splitting power properties are possible to be kept equal. This architecture also consists on creating two 90° phase shifter inside the MM.

Bibliography

- [1] Lucas B. Soldano and IEEE Erik C. M. Pennings, Member. Optical multi-mode interference devices based on self-imaging: Principles and applications. *Journal of lightwave technology*, vol. 13(no. 4):pp. 615–627, 1995.
- [2] Seok-Hwan Jeong and Ken Morito. Compact optical 90 degrees hybrid employing a tapered 2x4 MMI coupler serially connected by a 2x2 MMI coupler. *Optics express*, vol. 18(no 5):pp. 4275–4288, 2010.
- [3] Seok-hwan Jeong and Ken Morito. Simple analytical calculation and experimental demonstration of optical 90 degrees hybrids based on tapered 2 x 4 and 2 x 2 multi-mode interference couplers. vol. 28(no. 1):pp. 159–164, 2011.
- [4] Pierre A Besse, Emilio Gini, Maurus Bachmann, and Hans Melchior. New 2 x 2 and 1x3 Multimode Interfere with Free Selection of Power Splitting Ratios. *Journal of Lightwave Technology*, vol. 14(no. 10):pp. 2286–2293, 1996.
- [5] David S Levy, Robert Scarmozzino, York M Li, and Richard M Osgood. A New Design for Ultracompact Multimode. *IEEE Photonics Technology Letters*, vol. 10(no. 1):pp. 96–98, 1998.
- [6] Giorgia Parca, Pedro Teixeira, and Antonio Teixeira. All-optical image processing and compression based on Haar wavelet transform. *Applied Optics*, vol. 52(no. 12):pp. 2932–2939, 2013.
- [7] L Almeida, N Kumar, G Parca, A Tavares, A Lopes, and A Teixeira. All-Optical image processing based on Integrated Optics. *International Conference on Transparent Optical Networks*, pages pp. 1–5, 2014.

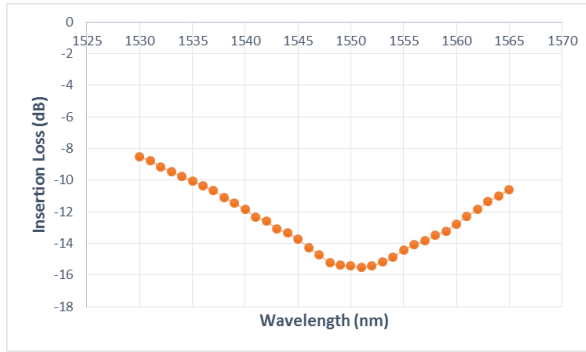
- [8] S El-Sabban, D Khalil, I Schanen, and P Benech. Design of an integrated optical magic T for astronomy applications. *Applied optics*, vol. 39(no. 36), 2000.
- [9] Guilherme Marieiro Cabral. All optical haar transform based on planar waveguides. Master’s thesis, Universidade de Aveiro, Departamento de Eletrónica, Telecomunicações e Informática, 2016.
- [10] Ginés Lifante. *Integrated Photonics Fundamentals*. Universidad Autónoma de Madrid, Spain, 2003.
- [11] T.H. Maiman. Stimulated optical radiation in ruby masers. *Nature*, vol. 187:pp. 493–494, 1960.
- [12] Design Manual VPIPhotonics. *MMI_M_N* , 2016.
- [13] H. F. Talbot. Facts relating to optical science. *London, Edinburgh Philosophical Mag., J. Sci.*, vol. 9(no. 4):pp. 401–407, December 1836.
- [14] Olof Bryngdahl. Image formation using self-imaging techniques. *Journal of the Optical Society of America*, (no. 4).
- [15] R. Ulrich. Image formation by phase coincidences in optical waveguides. *Optics Commun.*, vol. 13(no. 3):pp. 259–264, March 1975.
- [16] R. Ulrich. Light-propagation and imaging in planar optical waveguides. *Nouv. Rev. Optique*, vol. 6(no. 5):pp. 253–262, 1975.
- [17] David S Levy, Robert Scarmozzino, and Richard M Osgood. MMI Devices. *Technology*, vol. 10(no. 6):pp. 830–832, 1998.
- [18] Piotr Porwik and Agnieszka Lisowska. The Haar – Wavelet Transform in Digital Image Processing : Its Status and Achievements. *Machine GRAPHICS & VISION*, vol. 13:pp. 79–97, 2004.
- [19] V Ashok. The Fast Haar Wavelet Transform for Signal & Image Processing. vol. 7(no. 1):pp. 126–130, 2010.
- [20] Mark Nelson and Jean loup Gailly. Introduction to Data Compression. *The Scientist and Engineer’s Guide to Digital Signal Processing*, vol. 709(no. 4), 2013.

- [21] P.N. Topiwala. *Wavelet Image and Video Compression*, volume vol. 53. 1998.
- [22] Jeremy Iverson, Chandrika Kamath, and George Karypis. Fast & Effective Lossy Compression Algorithms for Scientific Datasets. *Europar*, 2012.
- [23] Amnon Yariv. Coupled-Mode theory for guided-wave optics. *IEEE Journal of Quantum Electronics*, vol. 9(no. 9):pp. 919–933, 1973.
- [24] Phoenix Software. User Manual OptoDesigner. (no 4.8.3), 2013.
- [25] Thanh T. Le and Laurence W. Cahill. The design of multimode interference couplers with arbitrary power splitting ratios on an SOI platform. *Conference Proceedings - Lasers and Electro-Optics Society Annual Meeting-LEOS*, pages pp. 378–379, 2008.
- [26] Trung-thanh Le. The Design of Optical Signal Transforms Based on Planar Waveguides on a Silicon on Insulator Platform. *International Journal of Engineering (IACSIT)*, vol. 2(no. 3):pp. 245–251, 2010.
- [27] Giovanni Gilardi and M.K. Smit. Generic InP-Based Integration Technology : Present and Prospects. *Progress In Electromagnetics Research*, vol. 147(February):pp. 23–35, 2014.
- [28] Jeppix Semi-commerical Access, Version Development, H H I Receiver, and Platform July. JePPIX - PARADIGM / EuroPIC Design Manual. 2014.
- [29] P. A. Besse M. Bachmann and H. Melchior. General self-imaging properties in $n \times n$ multimode interference couplers including phase relations. *Applied Optics*, vol. 33(no. 18):pp. 3905–3911, June, 1995.
- [30] M. Blahut and A. Opilski. Multimode interference structures - a new way of passive elements techonology for photonics. *Opto-Electronics review*, vol. 9(no 3):pp. 293–300, 2001.

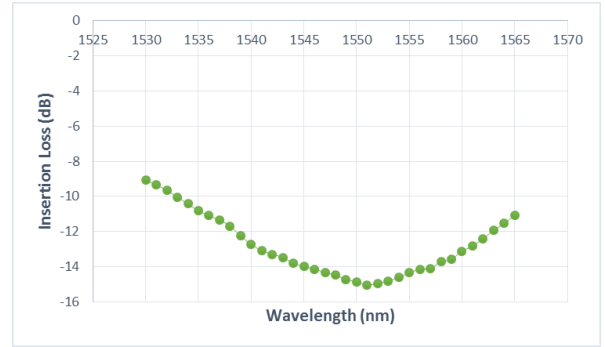
Appendix A

MMI 2 x 2 with access waveguide length change

Looking over the overlap power for a linear MMI with the waveguide length $L_w = 3\lambda_{5.599}$, figure A.1a and A.1b, we can observe a slightly improvement.



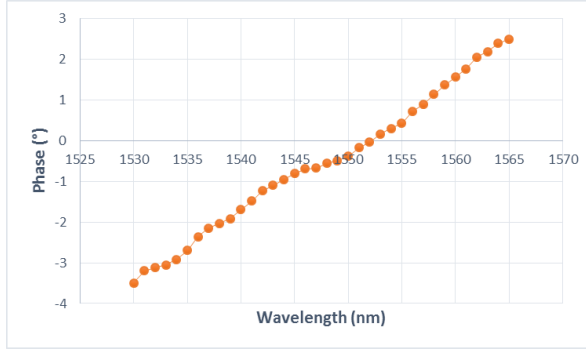
(a) Upper port as input



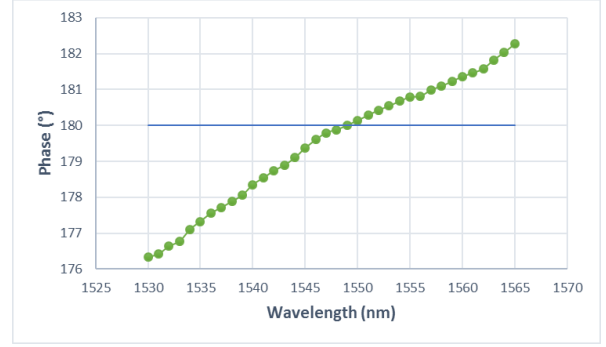
(b) Bottom port as input

Figure A.1: Linear MMI Insertion Loss

When referring the phase values through the C-band range, the maximum oscillating phase change it becomes $\approx 4^\circ$. In the figure A.2a and A.2b we can observe the swipe through the C-band and the phase behaviour for both outputs.



(a) Upper port as input



(b) Bottom port as input

Figure A.2: Linear MMI phase performance

As an overall, with both input ports working, we can verify, figure A.3, that the maximum loss ratio also slightly better. But this power improvement does not compensate the phase variations that with have with this length.

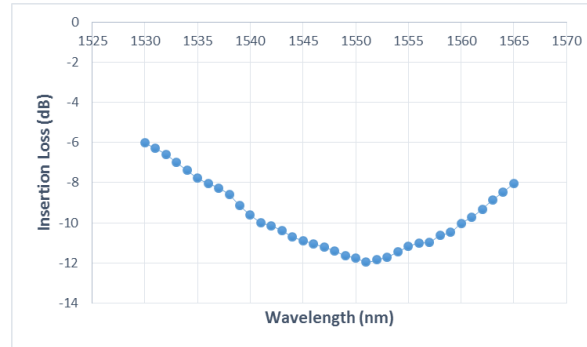


Figure A.3: Overall Insertion Loss in C-band range

Appendix B

Future work MMI architecture

This architecture was not fully develop during this thesis. Besse [4] showed that it is possible to create a phase shifter by tilting the MM waveguide. Inspired on his idea the next MMI emerged.

As observe in figure B.1 the MMI is symmetric and has two referential angles that shape the design. This two angles are the fundamental of this design.

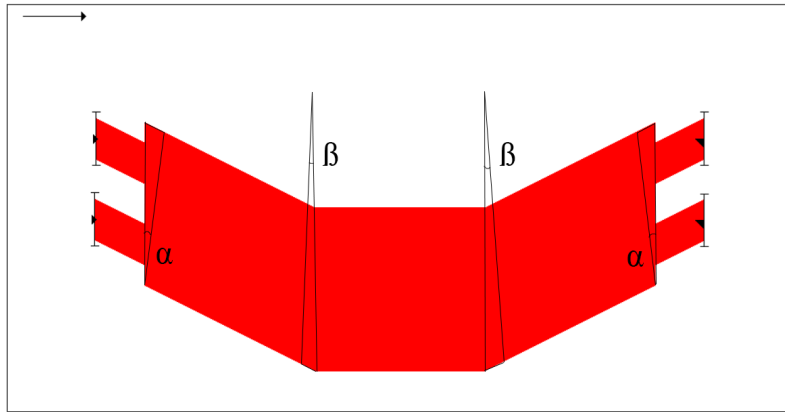


Figure B.1: Prototype MMI architecture design

With the angle β it is possible to implement the phase shifter inside the MM section, while with α it is possible to acquire the equal splitting power of 50/50.

The design was not fully implemented, the section created by angle α was not imple-

mented. In figure B.2 it is possible to verify the power propagation of the upper input, on the MM waveguide.

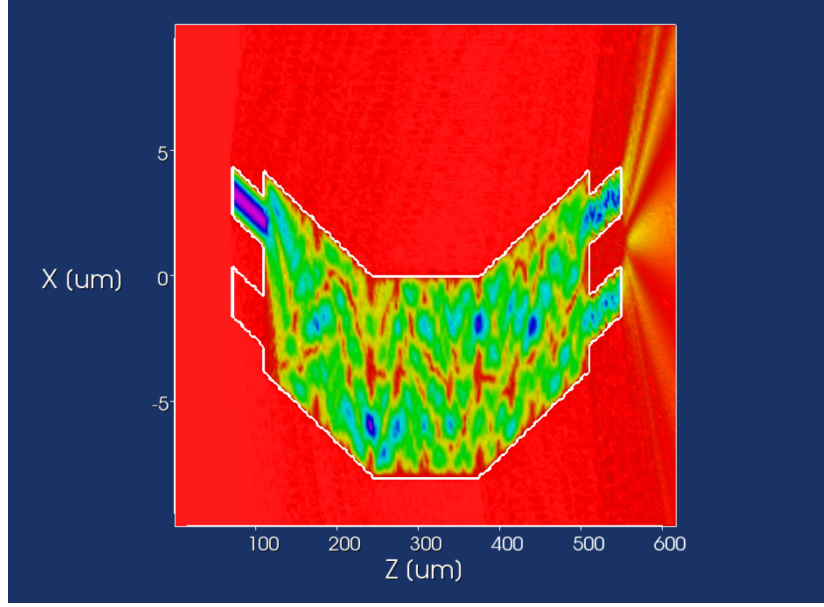


Figure B.2: Prototype design BPM simulation

The MMI parameters were not calculated. The output with two images was obtained by experimental mode. For a specific length, width and β values, the phase obtained at the outputs was equal for one input and 180° difference for the other input. The main problem observed was the power, because the split power was different from 50/50.